



High proportion strontium-doped micro-arc oxidation coatings enhance early osseointegration of titanium in osteoporosis by anti-oxidative stress pathway

Xinkun Shen¹, Kai Fang¹, Kendrick Hii Ru Yie, Zixin Zhou, Yiding Shen, Shuyi Wu, Yue Zhu, Zhennan Deng, Pingping Ma^{**}, Jianfeng Ma^{***}, Jinsong Liu^{*}

School and Hospital of Stomatology, Wenzhou Medical University, Wenzhou, 325027, China

ARTICLE INFO

Keywords:
Osteoporosis
Oxidative stress
Strontium
Osteoimmunomodulation
Osteogenesis

ABSTRACT

The excessive accumulation of reactive oxygen species (ROS) under osteoporosis precipitates a microenvironment with high levels of oxidative stress (OS). This could significantly interfere with the bioactivity of conventional titanium implants, impeding their early osseointegration with bone. We have prepared a series of strontium (Sr)-doped titanium implants via micro-arc oxidation (MAO) to verify their efficacy and differences in osteoinduction capabilities under normal and osteoporotic (high OS levels) conditions. Apart from the chemical composition, all groups exhibited similar physicochemical properties (morphology, roughness, crystal structure, and wettability). Among the groups, the low Sr group (Sr25%) was more conducive to osteogenesis under normal conditions. In contrast, by increasing the catalase (CAT)/superoxide dismutase (SOD) activity and decreasing ROS levels, the high Sr-doped samples (Sr75% and Sr100%) were superior to Sr25% in inducing osteogenic differentiation of MC3T3-E1 cells and the M2 phenotype polarization of RAW264.7 cells, thus enhancing early osseointegration. Furthermore, the results of both *in vitro* cell co-culture and *in vivo* studies also showed that the high Sr-doped samples (especially Sr100%) had positive effects on osteoimmunomodulation under the OS microenvironment. Ultimately, the collated findings indicated that the high proportion Sr-doped MAO coatings were more favorable for osteoporosis patients in implant restorations.

1. Introduction

Famed for its excellent biocompatibility and mechanical properties, titanium (Ti) has been widely utilized in dental implants. Along with the high success rate of implantation and considerable potential in osseointegration when used in healthy individuals, Ti implants have now become the cornerstone for edentulous restorations. However, when under the influence of certain diseases such as osteoporosis, the osseointegration potential of Ti implants may be severely impeded [1,2]. This is attributable to the pathophysiology of osteoporosis, causing weakening and disintegration of the bone mass in the jaw and hence has been considered to be contradictory to implant restorations [3,4]. Furthermore, having affected more than 200 million people in China

alone, the ever-rising incidence of osteoporosis is directly correlated with the significant rise in the aging population and life expectancy [5]. What's more, the patients to clinical implant repair are mostly middle-age and elder people, which are highly overlapped with osteoporosis patients. Consequentially, it is necessary to explore different methods in enhancing the early osseointegration and long-term success rate of implants under osteoporosis.

Studies have shown that cellular functions are extremely dependent on the surrounding microenvironment (extracellular matrix, body fluid components, etc.). Conversely, failure in preserving the homeostatic stability of the microenvironment will very likely lead to abnormal changes of cells/tissues [6,7]. A previous study has verified that patients with osteoporosis exhibit higher levels of oxidative stress (OS) when

Peer review under responsibility of KeAi Communications Co., Ltd.

* Corresponding author. 268# Xueyuan West Road, Lucheng District, Wenzhou City, Zhejiang Province, China.

** Corresponding author. 268# Xueyuan West Road, Lucheng District, Wenzhou City, Zhejiang Province, China.

*** Corresponding author. 268# Xueyuan West Road, Lucheng District, Wenzhou City, Zhejiang Province, China.

E-mail addresses: ppma2012@sina.com (P. Ma), dentistmacn@aliyun.com (J. Ma), jinsong0719@wmu.edu.cn (J. Liu).

¹ Co-first author: Xinkun Shen and Kai Fang contributed equally to this work.

<https://doi.org/10.1016/j.bioactmat.2021.08.031>

Received 6 June 2021; Received in revised form 24 August 2021; Accepted 27 August 2021

Available online 1 September 2021

2452-199X/© 2021 The Authors. Publishing services by Elsevier B.V. on behalf of KeAi Communications Co. Ltd. This is an open access article under the CC

BY-NC-ND license (<http://creativecommons.org/licenses/by-nc-nd/4.0/>).

compared to the healthy population [8]. Moreover, excessive accumulation of oxidant intermediates will have adverse effects on both the immune and skeletal systems of the body, exacerbating bone loss and impeding implant osseointegration [8,9]. For that reason, studies have suggested that the inhibition of excess accumulation of reactive oxygen species (ROS) can significantly augment bone mass [10,11]. Therefore, the negative regulation of osteoporosis-induced endogenous ROS is expected to become a more feasible approach to promote bone growth and osseointegration potential of Ti implants.

Surface antioxidant coating preparation is regarded as one of the more promising methods in endowing titanium implants with superior antioxidant properties. Previous studies have shown that under OS conditions, the anodized nanotopologies on Ti implants have superior antioxidant potential and are more conducive to osteogenesis compared to untreated Ti [12,13]. In recent years, a plethora of functional polymer coatings (e.g., silk fibroin, proanthocyanidin, etc.) are utilized in the development of antioxidant titanium implants [14,15]. However, the poor mechanical stability of the aforementioned anodic oxidation and polymer coatings limits their clinical application prospects. For this reason, the micro-arc oxidation (MAO) technique has seen a rise in popularity among researchers to be used as an alternative. Recently, it is demonstrated that MAO results in the formation of a porous oxide layer on implant surfaces, further enhancing biocompatibility and bonding strength [16]. Furthermore, by adjusting the electrolyte compositions, various metal ion-doped coatings can be successfully constructed onto implant surfaces [17]. Various metal ions (e.g., Mn, Cu, Sr, etc.) have been shown to possess good antioxidant properties, however, most of them are rarely studied [18–20], suggesting a multitude of possibilities in exploiting the benefits of these metal ions to fabricate Ti implant coatings.

Strontium (Sr), as an essential micro-element, has been proven to be an integral feature in the development of bone and/or teeth. Sr-doped implants are proved to significantly promote early osseointegration in both normal and osteoporotic conditions [21,22]. Previous studies on the mechanism of Sr²⁺ promoting bone formation mainly focused on the inhibition of osteoclast maturation and the promotion of osteoblast differentiation [23,24]. However, the relevant molecular mechanisms have not been fully understood, particularly during osteoporosis. Recently, Zhou et al. discovered that the Sr-doped titanium samples could significantly promote osteogenesis by decreasing ROS expression, inhibiting adipogenic differentiation of mesenchymal stem cells in aging rats [25]. With that said, the exploitation of the anti-oxidative stress mechanism of Sr-doped implants may be the key to realize its anti-osteoporosis potential.

That being said, however, Sr is demonstrated to be heavily dose-dependent. A low dose of Sr is proven to be conducive to osteogenesis and in contrast, a high dose of Sr will be detrimental to the surrounding microenvironment, causing cellular apoptosis [26,27]. Yan et al. discovered that the preparation of a Ti surface calcium phosphate coating composed of approximately 20% Sr was the most optimal in inducing osteogenesis in normal rat models [28]. However, with our limited understanding in regards to the effects of Sr and its dosage at the molecular level, it is uncertain whether 20% of Sr will be adequate in alleviating and preventing the harmful effects of osteoporosis. This may be one of the crucial factors in determining the osteogenic efficacy of related implant materials. Therefore, it is imperative to carry out in-depth investigations to further elucidate the bioactivities and potential mechanism of different Sr-doped biomaterials under normal and OS conditions.

In this study, we have fabricated a series of Sr-incorporated Ti substrate coatings via MAO and conducted an in-depth investigation into their dose-influenced osteogenic and antioxidant potential under normal and OS microenvironments. Following our previous study, an *in vitro* cell OS-injury model was established by adding 300 μM of hydrogen peroxide (H_2O_2) into the culture medium [29]. Herein, the following three issues are expected to be explored: 1) to study the osteoinductive

potential of the different proportions of Sr-doped MAO samples under normal and OS conditions; 2) to explore the relevant mechanisms behind the anti-oxidative stress capabilities of various Sr-doped Ti substrates; 3) to verify the viability of Sr-doped Ti equipped with the optimal antioxidant properties for osteoporosis-influenced implant restorations.

2. Materials and methods

2.1. Sample preparation and characterization

2.1.1. Sample preparation

Commercial Ti pieces (width: 10 mm, thickness: 2 mm) and Ti rods (diameter: 1.5 mm, length: 10 mm) were purchased from Northwest Institute for Nonferrous Metal Research (Xi'an, China). According to Table S1, different electrolytes containing $\text{Sr}(\text{CH}_3\text{COO})_2$, $\text{Ca}(\text{CH}_3\text{COO})_2$, and $\text{C}_3\text{H}_7\text{Na}_2\text{O}_6\text{P}\cdot 5(\text{H}_2\text{O})$ with different concentrations were first prepared under magnetic stirring. Afterward, a series of Sr-doped samples (Sr0%, Sr25%, Sr50%, Sr75% and Sr100%) were prepared in the corresponding electrolyte by MAO technique (Fig. 1A). Briefly, the cleaned Ti and platinum substrates were used as anode and cathode, respectively. The MAO process was carried out under a constant voltage mode at 550 V for 15 min. The duty cycle and frequency were 15% and 1000Hz, respectively. During the process, a circulating flow of cold water was used to lower the temperature of the electrolyte. After MAO treatment, the specimens were cleaned through immersion in distilled water for 30 s under ultrasonication.

2.1.2. Sample characterization

The surface morphology and roughness of specimens were characterized by scanning electron microscopy (SEM, Zeiss AURIGA FIB, Germany) and atomic force microscopy (AFM, Dimension, Bruker, Germany). The elemental compositions of the coatings were analyzed via an energy dispersive X-ray microanalysis system (EDS, Zeiss AURIGA FIB, Germany) and X-ray photoelectron spectroscopy (XPS, Model PHI 5400, Perkin Elmer, USA). The crystalline phases and wettability analysis of different samples were determined by X-ray diffraction (XRD, D/Max 2500 PC, Rigaku, Japan) and contact angle measuring instrument (DSA30, Kruss, Germany), respectively.

2.2. Osteoblast experiments *in vitro*

2.2.1. Endogenous ROS expression

MC3T3-E1 cells (1×10^4 cells/cm²) were cultured onto different samples for 3 d in α -Minimum Essential Medium (α -MEM, Hyclone) supplemented with 300 μM of hydrogen peroxide (H_2O_2) [13,29]. After fixation in 4% fixative solution (Solarbio Co.) for 30 min, MC3T3-E1 cells were stained using Reactive Oxygen Species Assay Kit (Beyotime Biotechnology Co.), and then observed through a confocal laser scanning microscope (CLSM, Nikon DS-Ri2, Nikon Instruments Inc., Japan). The CLSM instrument was equipped with a 16-megapixel color camera. The excitation/emission wavelengths ($\lambda_{\text{ex}}/\lambda_{\text{em}}$) of 2',7'-Dichlorodihydrofluorescein diacetate (DCFH-DA) dye were 488/525 nm. Moreover, the applied Amplification/Numerical Aperture (NA) of the objective lens were $20 \times /0.50$. Finally, the fluorescence intensity was quantitatively analyzed using Image-Pro Plus software.

2.2.2. Antioxidant enzyme activity

MC3T3-E1 cells (1×10^4 cells/cm²) were cultured in an H_2O_2 -supplemented medium for 3 d. Samples were rinsed 3 times using phosphate buffered saline (PBS), then 200 μL of sodium dodecyl sulfate (SDS) lysis buffer was added to each well and shook for 5 min. The catalase (CAT) and superoxide dismutase (SOD) in different groups was then determined by Catalase Assay Kit (Beyotime Biotechnology Co.) and Total Superoxide Dismutase Assay Kit (Beyotime Biotechnology) according to the instructions. Their absorbance was finally measured at 520 nm and

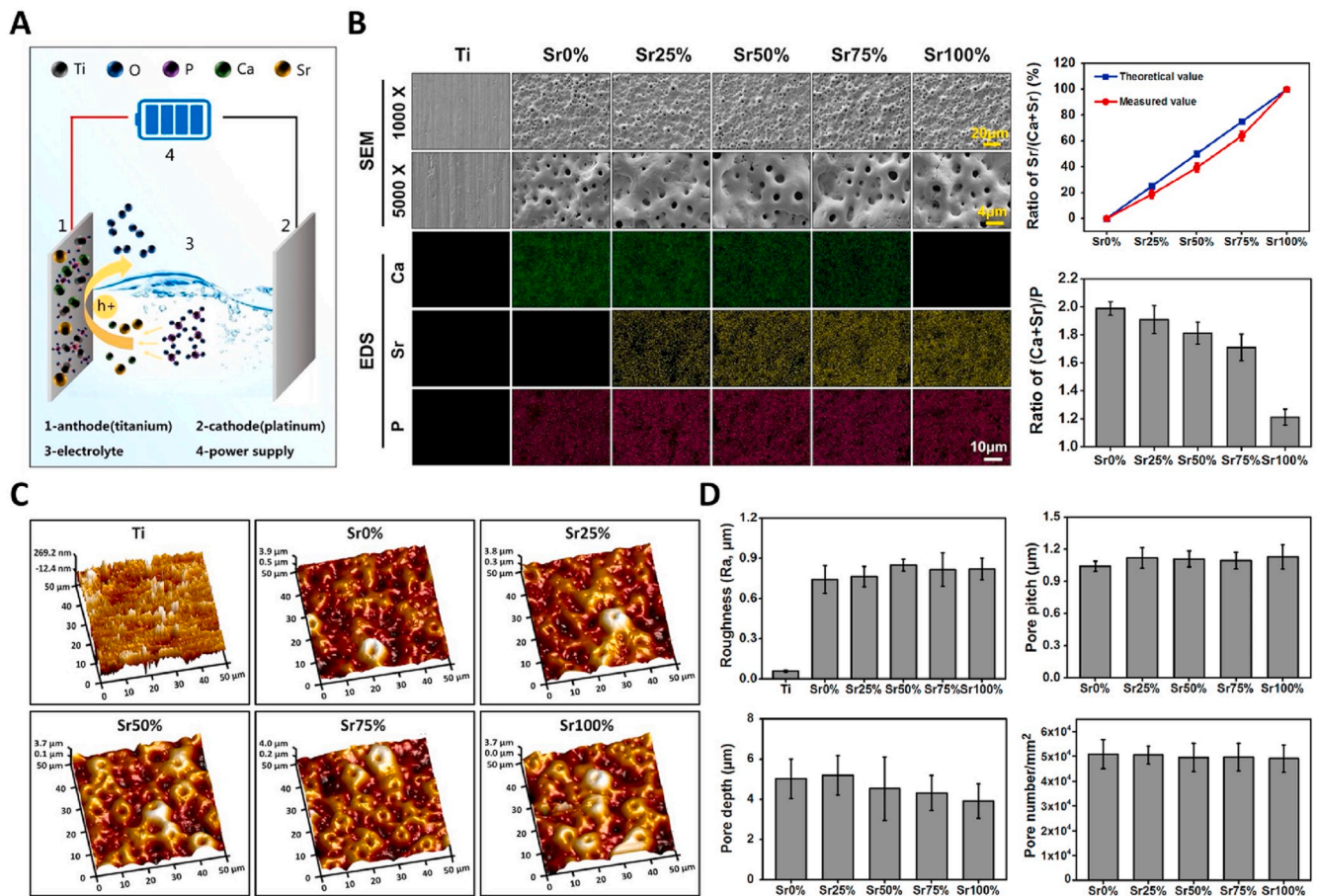


Fig. 1. Surface physicochemical properties: (A) schematic diagram of micro-arc oxidation treatment; (B) representative SEM/EDS images and corresponding ratios of Sr/(Sr + Ca) and (Sr + Ca)/P; (C) AFM images of different samples; (D) quantitative statistics of surface roughness and pore pitch/depth/number according to the above AFM images.

450 nm using a microplate reader (Multiskan Spectrum, Thermo Fisher Scientific Inc., USA), respectively.

2.2.3. Cell morphology

MC3T3-E1 cells (1×10^4 cells/cm²) were cultured in an H₂O₂-supplemented medium for 3 d. The adherent cells were then fixed with 4% fixative solution and perforated with 0.2% Triton-X solution (Beyotime Biotechnology Co.). After that, the fixed cytoskeleton and nucleus were stained with tetramethylrhodamine (TRITC) phalloidin (Solarbio Co.) and 4',6-diamidino-2-phenylindole (DAPI, Solarbio Co.), and observed by a CLSM. The $\lambda_{\text{ex}}/\lambda_{\text{em}}$ of TRITC-phalloidin and DAPI dyes were 540/565 and 358/461 nm, respectively. The applied Amplification/NA of the objective lens were $20 \times /0.50$.

2.2.4. Cell viability

MC3T3-E1 cells (1×10^4 cells/cm²) were cultured in both normal or H₂O₂-supplemented medium for 3 d. The mixture solution of medium and tetrazolium bromide (MTT, Solarbio Co.) was added to each well and incubated for another 4 h. Dimethyl sulfoxide (DMSO) was then used to dissolve the formed formazan crystals. 200 μL of the dissolved solution was collected to measure the optical density (OD) value with a microplate reader at 490 nm.

2.2.5. Alkaline phosphatase (ALP) activity

MC3T3-E1 cells (1×10^4 cells/cm²) were cultured in both normal and H₂O₂-supplemented medium for 7 d, separately. For ALP staining, the adherent cells were firstly immobilized with 4% fixative solution, stained with 5-Bromo-4-Chloro-3-Indolyl Phosphate/Nitroblue

tetrazolium chloride (BCIP/NBT) Alkaline Phosphatase Color Development Kit (Beyotime Biotechnology Co.), and then observed under a stereomicroscope. For ALP activity detection, cells were first lysed with 1% Triton-X solution. Then, 200 μL of lysate from each group was collected to measure the ALP activity and total protein concentration using Alkaline Phosphatase Assay Kit (Nanjing Bioengineering Institute) and Bicinchoninic Acid (BCA) Protein Assay Kit (Beyotime Biotechnology Co.). Their OD values were measured using a microplate reader at 520 and 562 nm, respectively.

2.2.6. Collagen secretion

MC3T3-E1 cells (1×10^4 cells/cm²) were cultured in both normal and H₂O₂-supplemented medium for 14 d, separately. After fixation of adherent cells with 4% fixative solution, they were stained using Sirius red dye (Solarbio Co.) and visualized under a stereomicroscope. Finally, the stained collagen crystals were dissolved in 0.1 M NaOH solution and detected using a microplate reader at 540 nm.

2.2.7. Osteocalcin (OCN) expression

MC3T3-E1 cells (1×10^4 cells/cm²) were cultured in an H₂O₂-supplemented medium. On the 14th day, supernatant of each cell culture medium was collected. The concentration of OCN in each group was measured with an enzyme-linked immunosorbent assay kit (Biomedical Technologies Inc.) according to the instruction. The OD value of the final solution was determined by a microplate reader at 450 nm.

2.2.8. Osteogenic gene expression

MC3T3-E1 cells (1×10^4 cells/cm²) were cultured in an H₂O₂-

supplemented medium for 7 d. The total RNA was extracted using an RNA simple Total RNA Kit (Tiangen Biotech Co.) following the provided protocol. The PrimeScript RT reagent Kit with gDNA Eraser (Takara Bio Inc.) and SYBR Premix EX Taq kit (Takara Bio Inc.) were then used to prepare the first-strand cDNA. Quantitative reverse transcription PCR (RT-qPCR) analysis was utilized for the detection of the following target genes: runt-related transcription factor 2 (Runx2), ALP, collagen type I (COL I), bone sialoprotein (BSP), osteopontin (OPN) and OCN. The primer sequences are listed in Table S2.

2.3. Macrophage experiments *in vitro*

2.3.1. Endogenous ROS expression

RAW264.7 cells (5×10^4 cells/cm²) were seeded onto the different substrates and cultured in Dulbecco's Modified Eagle Medium (DMEM, Hyclone, high glucose) supplemented with 300 μ M of H₂O₂. After 3 d, the expression of endogenous ROS in RAW264.7 cells was measured following an aforementioned experimental protocol with reference to section 2.2.1.

2.3.2. Antioxidant enzyme activity

RAW264.7 cells (5×10^4 cells/cm²) were cultured in an H₂O₂-supplemented medium for 3 d. Then, the CAT and SOD activity of RAW264.7 cells on different substrates were detected with reference to section 2.2.2.

2.3.3. Cell morphology

RAW264.7 cells (5×10^4 cells/cm²) were cultured in an H₂O₂-supplemented medium for 3 d. The morphology (cytoskeleton and nucleus) of cells was visualized through fluorescence staining with reference to section 2.2.3. The applied Amplification/NA of the objective lens were $40 \times /0.75$. Based on the fluorescence results, the normalized cell area and circularity were then calculated using Image-Pro Plus software. Moreover, for SEM observation, the adherent cells were fixed with a 4% fixative solution and dehydrated with gradient ethanol. After gold spray treatment, the cell morphology was further evaluated by SEM.

2.3.4. Gene expression

RAW264.7 cells (5×10^4 cells/cm²) were cultured in an H₂O₂-supplemented medium for 3 d. Next, RT-qPCR was utilized to detect several inflammation-specific genes: cluster of differentiation 206 (CD206), C–C chemokine receptor type (CCR7), arginase-1 (Arg), inducible nitric oxide synthase (iNOS), interleukin 10 (IL-10), interleukin 1 receptor antagonist (IL-1ra), interleukin 6 (IL-6), tumor necrosis factor alpha (TNF α), transforming growth factor beta (TGF β), and bone morphogenetic protein 2 (BMP2), following the same experimental protocol with reference to section 2.2.8. The primer sequences are listed in Table S2.

2.3.5. Expression of inflammatory factors

RAW264.7 cells (5×10^4 cells/cm²) were cultured in an H₂O₂-supplemented medium for 3 d. The culture medium was then collected and Mouse IL-10 Quantikine ELISA Kit (R&D Systems Co.) as well as Mouse TNF- α Quantikine ELISA Kit (R&D Systems Co.) were utilized for the detection of the concentration of anti-inflammatory IL-10 and pro-inflammatory TNF α concentration, respectively. Subsequently, their OD values were measured using a microplate reader at 450 nm and 540 nm, respectively.

2.4. Co-culture of macrophage and osteoblast *in vitro*

The medium of RAW264.7 cells cultured on different Ti-based substrates for 3 d was collected as conditional medium, which was then used to culture MC3T3-E1 cells directly seeded on cell culture plate (Fig. 5A). Referring to sections 2.2.4–2.2.6 and 2.2.8, the cell viability (3 d), ALP activity (7 d), collagen secretion (14 d) and osteogenic gene expression (7 d) of the co-cultured MC3T3-E1 cells were performed. In addition, the

mineralization of MC3T3-E1 cells at 14 d was also detected. Briefly, after immobilization of adherent cells with 4% fixative solution, the cells were stained using alizarin red dye (Solarbio Co.) and visualized under a stereomicroscope. Next, the stained calcium nodules were dissolved in 10% cetylpyridinium chloride solution and detected using a microplate reader at 540 nm.

2.5. Animal experiments

2.5.1. Establishment and implantation of osteoporosis animal model

Fifty female Sprague-Dawley rats (~200 g), provided by Wenzhou Medical University, were randomly divided into normal [Sr25% (n = 5) & Sr100% (n = 5)] and osteoporotic groups [Ti (n = 10), Sr0% (n = 10), Sr25% (n = 10) & Sr100% (n = 10)]. All conducted animal experiments were approved by the ethics committee of Wenzhou Medical University [SYXK (Zhe) 2019-0009]. According to the previous study, all rats underwent bilateral ovariectomy in order to establish the osteoporosis model [30]. Subsequently, the different Ti implants were implanted into the femoral epiphysis of both normal and osteoporotic rats.

2.5.2. Macrophage polarization

After implantation for 7 d, three osteoporotic rats in each group were sacrificed and their femurs were collected. The extracted femurs were fixed using 10% formalin for 24 h before decalcification, gradient alcohol dehydration, and xylene transparency treatment. Chengdu Lilai Biological Technology Co., Ltd. was commissioned to prepare paraffin sections of the femurs for a following immunofluorescence staining analysis. The expression of arginase I (Arg, M2 macrophage marker), inducible Nitric oxide synthase (iNOS, M1 macrophage marker), and CD68 (monocyte marker) proteins were detected by specific Arg (Proteintech Group, Inc.), iNOS (Proteintech Group, Inc.) or CD68 (Santa Cruz Biotechnology, Inc.) monoclonal antibodies and fluorescein isothiocyanate (FITC)/TRITC-labeled fluorescent second antibodies, respectively. The Nuclei of the tissues were further stained with DAPI staining solution. The $\lambda_{ex}/\lambda_{em}$ of FITC, TRITC, and DAPI dyes for CLSM detection were 495/513, 540/565 and 358/461 nm, respectively. The applied Amplification/NA of the objective lens were $10 \times /0.30$. Finally, we collated the data obtained from the company and further quantitated the analysis.

2.5.3. Oxidative stress level

To investigate the OS level around different implants, after 6 d, 25 mg/kg of dihydroethidium (DHE, Sigma Chemical Co.) fluorescence dye was intravenously administered into the osteoporotic rats (two rats in each group) [30]. A day after, the rats were sacrificed and their femurs removed, followed by decalcification procedure using a mixture of 100 mL nitric acid, 150 mL formaldehyde, and 750 mL deionized water under dark condition. Subsequently, the femurs were dehydrated with gradient sucrose solutions and embedded using optimum cutting temperature compound (SAKURA Tissue-Tek®) in a cryostat (LEICA CM1950, Leica Biosystems, German). Finally, the samples were sectioned, observed under CLSM ($\lambda_{ex}/\lambda_{em}$: 300/610 nm; Amplification/NA: $10 \times /0.30$), and quantitatively analyzed using Image-Pro Plus software.

2.5.4. Local osteogenesis

After 1 month, the remaining normal and osteoporotic rats (five rats in each group) were sacrificed and their femur removed. The collected samples were fixed 10% formalin solution prior to histochemical double-staining of hematoxylin-eosin (HE) and Masson trichrome for the detection of new bone mass and bone maturity around different implants. With reference to section 2.5.3, Chengdu Lilai Biotechnology Co., Ltd. was commissioned to prepare the paraffin sections of the samples for staining and visualization after decalcification, gradient alcohol dehydration and xylene transparency treatment. Furthermore, we utilized the micro-computed tomography system (micro-CT, Skyscan1176,

Bruker, Germany) for further verification of new bone formation around the implants. CTAn software was used to quantify and analyze the ratio of new bone volume/total volume (BV/TV), trabeculae number (Tb.N), trabeculae thickness (Tb.Th), and trabeculae space (Tb.Sp). The analysis area for the new bone formation was set to a 0.5 mm radius around the implant.

2.6. Statistical analysis

All experiments were conducted with a minimum of 3 repetitions. Initially, the Kolmogorov-Smirnov (K-S) test was employed to ensure that all data conformed to the normal distribution. All of the data were then applied to the final charting and presented as means \pm standard deviation. Because there was only one variable (various experimental samples) throughout the whole statistical analysis procedure in this work, the gathered data were evaluated through Student's t-test and one-way analysis of variance (ANOVA) using OriginPro software (version 8.5). A level of $*p < 0.05$ was considered to be statistically significant.

3. Result

3.1. Surface characterization

As depicted from the SEM images (Fig. 1B), pure Ti samples displayed a relatively smooth surface in both low and high magnification, whereas Sr-doped Ti samples displayed a sporadic formation of sponge-like pores on its surface with an average diameter of approximately 1.5 μm . Through EDS analysis (Fig. 1B & Table S3), we verified that the amount of P element in the various coatings were similar, however the amount of Ca element decreased and the proportion of Sr element increased with the increase of $\text{Sr}(\text{CH}_3\text{COO})_2$ concentration (from 0 to

0.2 mol/L). Moreover, we discovered that the ratio of Sr in several Sr/(Ca + Sr) groups (Sr25%, Sr50% and Sr75% groups) did not meet their expected/theoretical values (25%, 50%, 75% respectively), and the quantitative values were 19.2 ± 0.9 , 39.2 ± 0.4 and 63.8 ± 0.7 , respectively. The ratio of (Ca + Sr)/P also gradually decreased with the increase of initial $\text{Sr}(\text{CH}_3\text{COO})_2$: Sr0% (1.98 ± 0.05), Sr25% (1.91 ± 0.10), Sr50% (1.81 ± 0.08), Sr75% (1.70 ± 0.09), and Sr100% (1.21 ± 0.06). AFM images (Fig. 1C) further verified the presence of rough porous structures on the Ti surface of all groups apart from pure Ti samples. Their surface roughness was quantified at approximately 0.8 μm (Fig. 1D). Through in-depth analysis of AFM results, it was clear that the pitch ($\sim 1.1 \mu\text{m}$), depth ($\sim 4.5 \mu\text{m}$) and number ($\sim 5 \times 10^4$ pores/ cm^2) of all pore structures were similar (Fig. 1D).

As for the composition of the compounds in all MAO-treated samples, XPS analysis was further performed and the results were shown in Fig. 2 & S3. From the Ti2p data (Fig. 2A and D), we could observe the presence of three different Ti-related, notably the TiO_2 , $(\text{Sr}/\text{Ca})\text{TiO}_3$ and $\text{Ti}_3(\text{PO}_4)_4$ compounds on all Sr-incorporated (Sr25%, Sr50%, Sr75%, Sr100%) surfaces. The proportions for each compound, however, were different among the groups. The proportion of TiO_2 was similar in all groups at approximately 53%, meanwhile, $(\text{Sr}/\text{Ca})\text{TiO}_3$ compound decreased with the increase of Sr amount, whereas $\text{Ti}_3(\text{PO}_4)_4$ compounds increased correspondingly with the increase of Sr proportion. The split-fitting spectra of P2p (Fig. 2B and D) also followed a similar trend showing a decrease in $(\text{Sr}/\text{Ca})\text{TiO}_3$ and an increase in $\text{Ti}_3(\text{PO}_4)_4$. Next, the Sr3d data (Fig. 2C and D) displayed the presence of three Sr-related compounds, namely SrTiO_3 , $\text{Sr}_3(\text{PO}_4)_2$, and SrO. The proportion of SrTiO_3 compounds stayed relatively unchanged with the increase of Sr proportion. However, there was a decrease in $\text{Sr}_3(\text{PO}_4)_2$ and an increase in SrO at a higher concentration of Sr. Finally, the Ca2p data (Fig. S3) showed no significant differences in the ratios of $\text{Ca}_3(\text{PO}_4)_2$, CaO, or CaTiO_3 among the Sr25%, Sr50% and Sr75% groups.

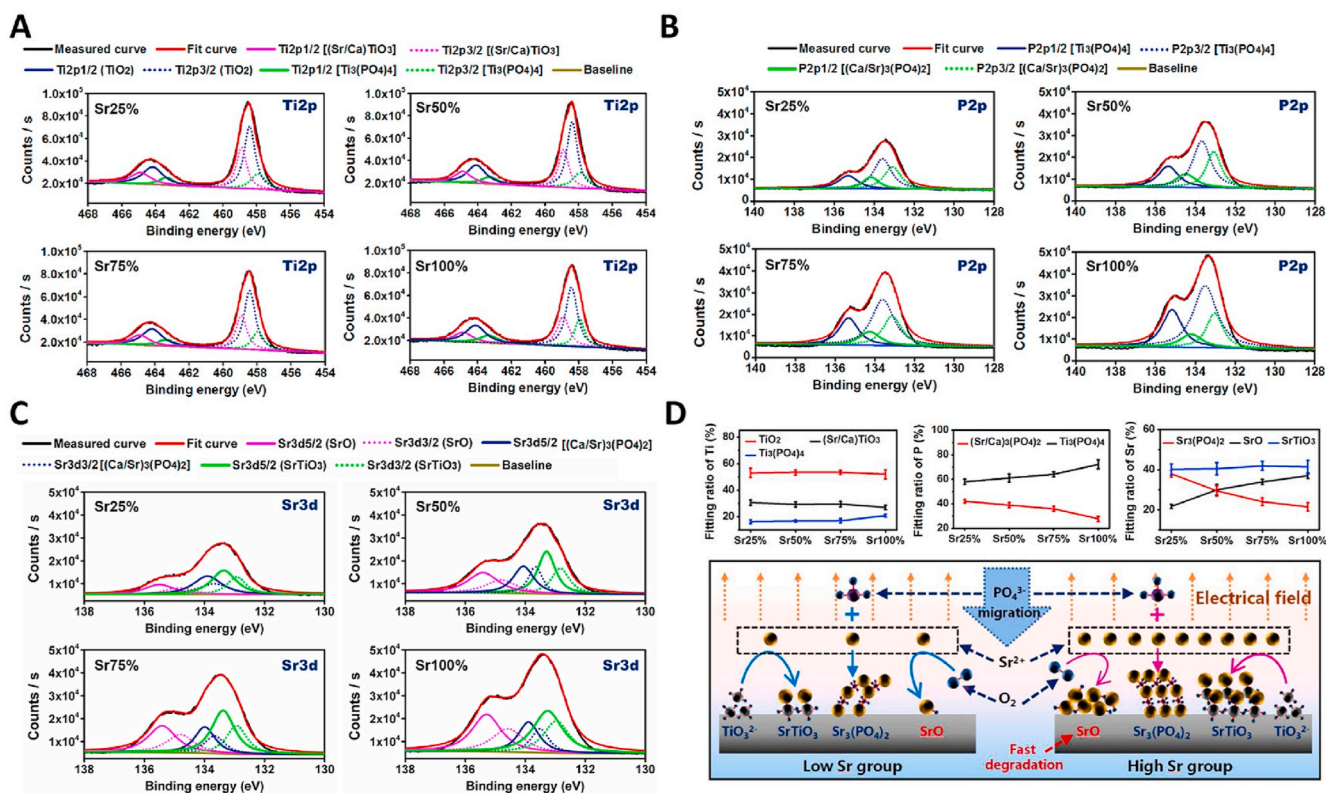


Fig. 2. Chemical composition of Sr-incorporated coatings: split-fitting spectra of Ti2p (A), P2p (B) and Sr3d (C) peaks in different samples (Sr25%, Sr50%, Sr75% & Sr100%) based on XPS data; (D) the proportion of different compounds containing Ti, P or Sr in various coatings and the formation diagram of Sr compounds [SrO , SrTiO_3 & $\text{Sr}_3(\text{PO}_4)_2$].

To further investigate the difference in the surface wettability and crystalline structures of the different samples, both WCA and XRD analyses were carried out. The quantified data are displayed in Fig. S1 & S2. The surface water contact angle of Ti was about 64.6°, and only Ti peak (JCPDS 05-0682) was detected on its surface. After MAO treatment, the surface contact angles of the five samples were around 7°, which were significantly less when compared to Ti. XRD analysis of post-MAO treated samples all showed similarity in their peaks, showing peaks of rutile (JCPDS 21-1276) and anatase (JCPDS 21-1272) at specific angles (rutile: 25.1, 37.6, 41.1 & 55.0°; anatase: 27.3, 35.9 & 53.8°). The collated results proved that apart from the physicochemical properties which were similar in all samples, the addition of high concentration of Sr²⁺ would alter the chemical composition of MAO coating (the only variable), especially the increase of water-soluble SrO.

The release evaluation of Sr²⁺ from Sr25% or Sr100% was displayed in Fig. S4. It was found that the release duration of Sr²⁺ from the samples of both groups exceeded 21 d. With the increase of soaking time, the release rate of ions gradually slowed down. However, the release rate and amount of Sr²⁺ in the Sr100% group were significantly higher than those of the Sr25% group. At the first, second, and third week, Sr²⁺ from Sr25% was released at a concentration of around 7.3, 2.2, 1.5 ppm, respectively. Meanwhile, a concentration of 17.8, 5.0, 3.2 ppm of Sr²⁺ were released from the Sr100% group, respectively.

3.2. Effects of different coatings on MC3T3-E1 cells

To evaluate the anti-oxidative stress potential of MC3T3-E1 cells on different substrates, the endogenous ROS levels and antioxidant enzyme activities were detected. Fig. 3A depicted a significant decrease in the fluorescence intensity of adherent cells with the increase of Sr doping: Ti ≈ Sr0% < Sr25% < Sr50% < Sr75% ≈ Sr100% (comparison of Ti and Sr25% groups: p < 0.05; comparison of Sr50% and Sr100% groups: p <

0.05; comparison of Ti/Sr0%/Sr25% and Sr50%/Sr75%/Sr100% groups: p < 0.05). Because the intensity reflects the degree of OS, the results suggested that the antioxidation capacity of high Sr groups (Sr75% & Sr100%) were better (p < 0.05) than that of the other groups. In contrast to the fluorescence intensity of ROS, the activities of the antioxidant enzymes (CAT & SOD) increased with the increase of Sr concentration (Fig. 3B). Compared to Ti and Sr0%, all samples in Sr25%, Sr50%, Sr75% and Sr100% groups significantly promoted CAT activity (p < 0.05), however, only the latter two groups effectively enhanced the activity of SOD. Moreover, we found that the CAT activity of MC3T3-E1 cells on Sr75% and Sr100% was significantly higher (p < 0.05) than that of the Sr25% group. From these data, we verified that high-dose Sr doping in MAO coatings had positive effects on the CAT and SOD activity of adherent osteoblasts, thus enhancing the antioxidant efficacy under OS conditions.

Cytological studies, including morphological observation, cell viability, ALP activity, collagen expression, OCN secretion, and osteogenic gene expression were carried out to assess the osteoinductive capacity of different samples under OS microenvironment (Fig. 3C–H). Fluorescent staining images (Fig. 3C) illustrated a similarity in the shrinking morphology of the cells in all six groups. MTT evaluation on the viability of MC3T3-E1 cells showed a corresponding increase in the cell viability with the increasing proportion of Sr²⁺ (Sr0% < Sr25% < Sr50% < Sr75%) when compared to pure Ti group. However, we could observe a slight decrease in cell viability in the Sr100% group (Fig. 3D). Although the cell viability results indicated that Sr25%, Sr50%, Sr75% and Sr100% groups were significantly better (p < 0.05) than that of the Ti group, no significant difference was found among the four groups. ALP activity (Fig. 3E & Fig. S6), collagen expression (Fig. 3F), and OCN secretion (Fig. 3G) results followed a similar trend to the cell viability data, validating Sr75% group to be the most optimal [ALP activity: comparison of Ti/Sr0%/Sr25% and Sr75% groups (p < 0.05); collagen

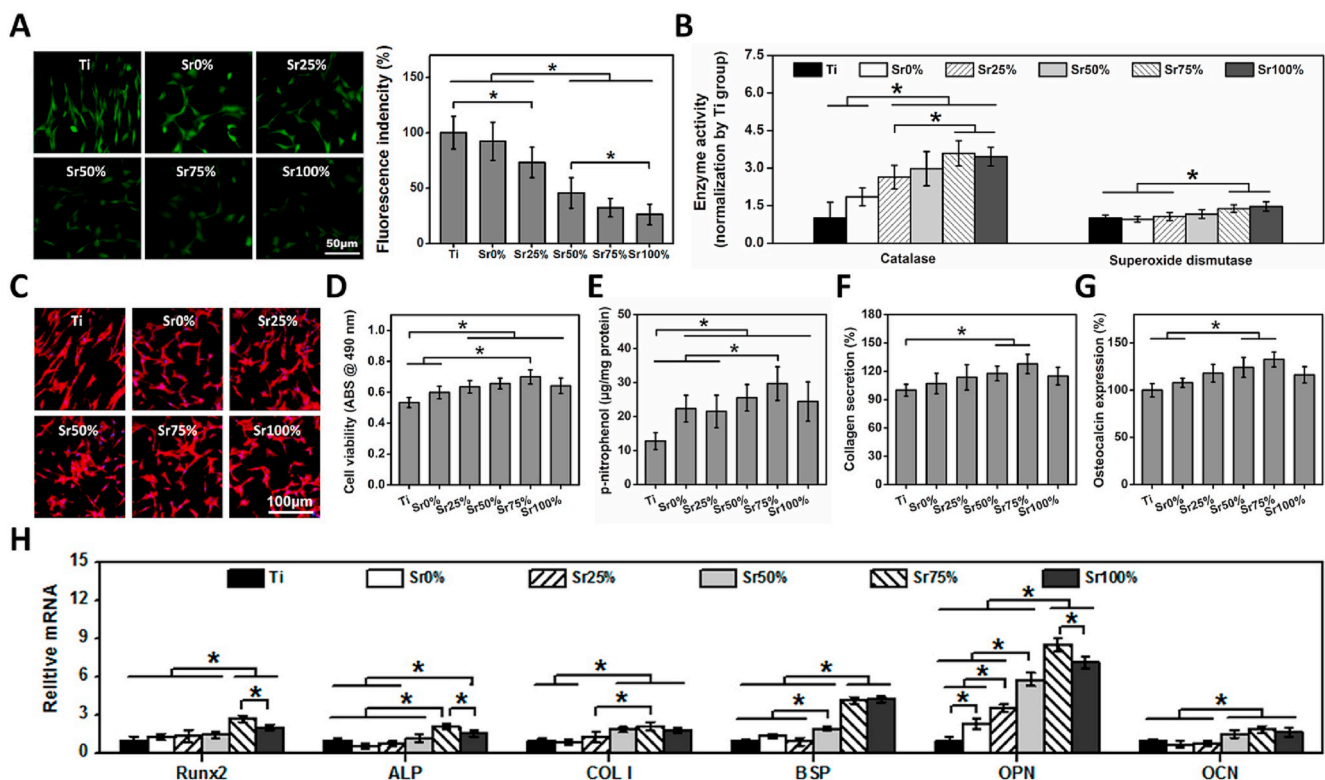


Fig. 3. *In vitro* assays of H₂O₂-stimulated MC3T3-E1 cells: (A) DCFH-DA staining images and the corresponding fluorescence intensity statistics; (B) SOD and CAT activities of the adherent cells on different substrates after 3 d; (C) representative staining images of cell morphology (red: cytoskeleton; blue: nucleus); quantitative statistics of cell viability (D), ALP activity (E), collagen secretion (F), and OCN secretion (G); (H) expression of some osteogenesis-related genes in different groups. Error bars represent mean ± SD for n = 6, *p < 0.05.

expression: comparison of Ti and Sr50%/Sr75% groups ($p < 0.05$); OCN secretion: comparison of Ti/Sr0% and Sr50%/Sr75% groups ($p < 0.05$)). We also discovered that the expression of the osteogenesis-related genes (Runx2, ALP, COL I, BSP, OPN & OCN) in high Sr groups (Sr75% or Sr100%) was significantly higher ($p < 0.05$) than that of Ti, Sr0% and Sr25% groups (Fig. 3H). In addition, compared with Sr100% group, the expression of Runx2, ALP and OPN genes were significantly ($p < 0.05$) increased in Sr75% group, but the expression of COL I, BSP and OCN genes showed no significant difference.

In order to compare the cellular behaviors under OS microenvironment, we conducted an in-depth investigation of the effects of different coatings on the proliferation and differentiation of MC3T3-E1 cells under normal conditions. From Fig. S5, we could also observe a similar trend in the cell viability, ALP activity, and collagen secretion of the adherent cells with that of OS-exposed cells, following an initial increase then decrease pattern with the increase of Sr²⁺ in the coatings. However, the optimal proliferation and osteogenic differentiation of MC3T3-E1 cells were observed in the Sr25% group. Compared with the Sr25% group, the biological functions of MC3T3-E1 cells in the Ti, Sr75% and Sr100% groups significantly decreased ($p < 0.05$).

The aforementioned results indicates that the biological activities of the various Sr-doped samples were different under normal and OS microenvironments. Under normal condition, low Sr samples (Sr25%) were the most conducive for the proliferation and osteogenic

differentiation of MC3T3-E1 cells. In contrast, high Sr materials (Sr75% and Sr100%) proved to be more beneficial to osteogenesis under OS microenvironment. This phenomenon may be linked to the increase of CAT/SOD activity and the decrease of endogenous ROS level.

3.3. Effects of different coatings on macrophages

The ROS expression and SOD/CAT activity analysis were carried out to assess the antioxidant ability of RAW264.7 cells on different Sr-doped substrates. DCFH-DA staining images and statistical results (Fig. S7A) showed that the green fluorescence intensity of the surface cells decreased with the increase of Sr in MAO coatings (comparison of Ti and Sr0% groups: $p < 0.05$; comparison of Ti/Sr0% and Sr25%/Sr50%/Sr75%/Sr100% groups: $p < 0.05$; comparison of Sr25%/Sr50% and Sr50%/Sr75% groups: $p < 0.05$). Similar to osteoblasts (Fig. 3A), this suggested that Sr²⁺ also enhanced the antioxidant capacity of macrophages. Next, from Fig. S7B, we also discovered that the activities of CAT and SOD increased correspondingly with Sr [SOD activity: comparison of Ti/Sr0% and Sr25%/Sr50%/Sr75%/Sr100% groups ($p < 0.05$), comparison of Sr25% and Sr100% groups ($p < 0.05$); CAT activity: comparison of Ti/Sr0%/Sr25% and Sr75%/Sr100% groups ($p < 0.05$), comparison of Ti and Sr50% groups ($p < 0.05$)], which may be one of the key factors in the improvement of antioxidant ability of RAW264.7 cells in the high Sr group (Sr75% & Sr100%).

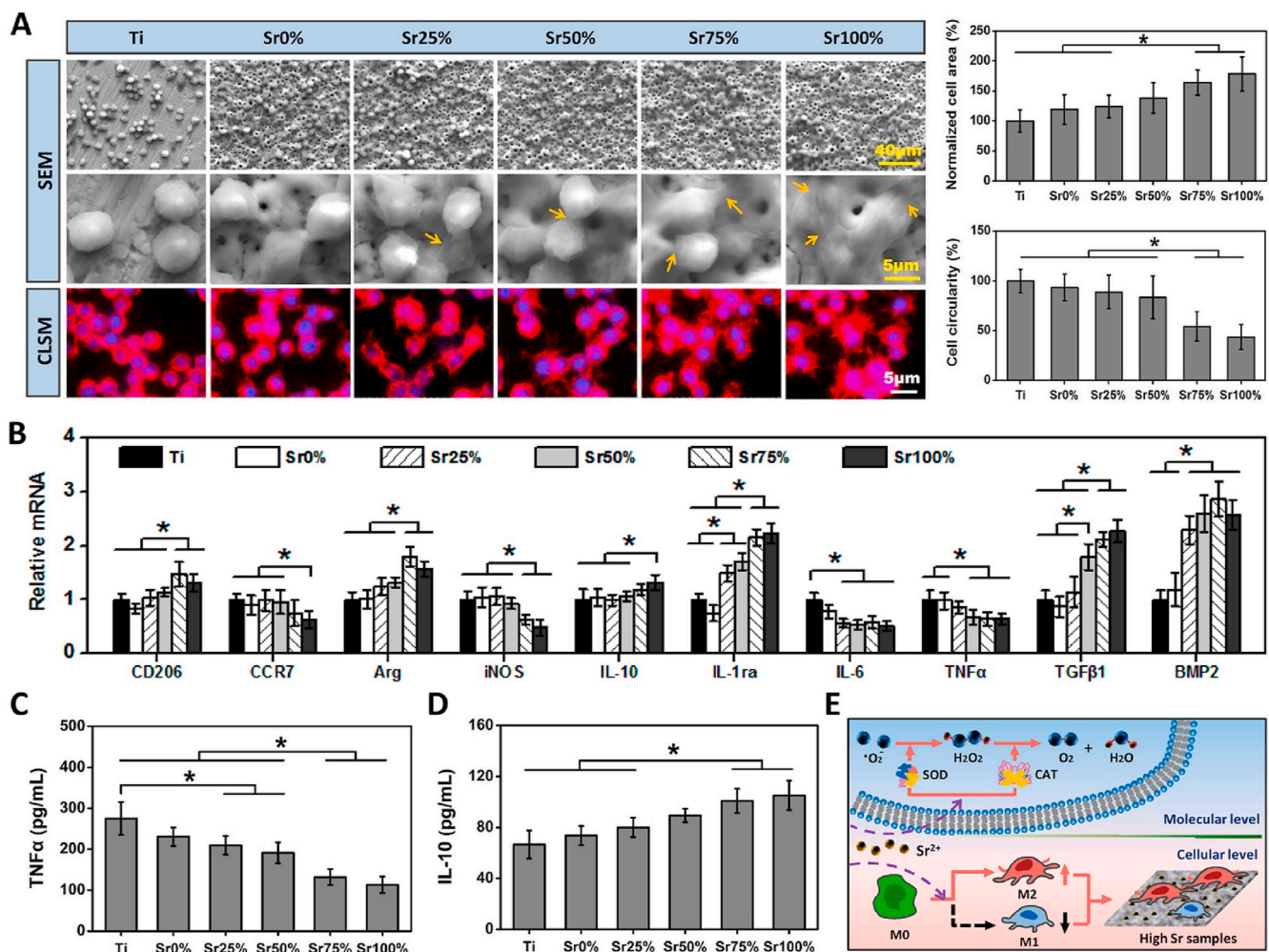


Fig. 4. *In vitro* assays of H₂O₂-stimulated RAW264.7 cells: (A) representative SEM/fluorescence images of cell morphology and quantitative statistics of cell area/circularity; (B) expression of genes related to cell polarization (M1 macrophage: CD206 & Arg; M1 macrophage: CCR7 & iNOS), inflammation (anti-inflammation: IL-10 & IL-1ra; pro-inflammation: IL-6 & TNFα) and osteogenesis (TGFβ1 & BMP2) in different groups; the concentration of TNFα (C) and IL-10 (D) in medium supernatant; (E) schematic diagram of phenotypic regulation by peroxidase pathway in high strontium group. Error bars represent mean ± SD for n = 6, *p < 0.05.

To investigate the phenotypic difference of RAW264.7 cells on different samples under OS, the cell morphology and gene/cytokine expression were studied. From SEM and CLSM images (Fig. 4A), we observed that RAW264.7 cells in Sr75% and Sr100% groups were in a spreading state, while the other four groups were spherical. The quantitative analysis further confirmed that the cell area and circularity of RAW264.7 cells in Sr75% and Sr100% groups were significantly ($p < 0.05$) different from those in the other four groups, showing an increased in cell area and a decrease cell circularity with the increase of Sr doping. Next, the gene expression (Fig. 4B) of both macrophage M2 phenotypic markers (CD206 and Arg) and M1 phenotypic markers (CCR7 and iNOS) in Sr75% and Sr100% groups were significantly higher ($p < 0.05$) and lower ($p < 0.05$), respectively, than those in Ti, Sr0%, Sr25% and Sr50% groups. The expression of anti-inflammatory (IL-10, IL-1ra) and osteogenic (TGF β 1, BMP2) related genes also increased in the high Sr groups (Sr75% & Sr100%). Furthermore, the expression of pro-inflammatory genes (IL-6, TNF α) was obviously inhibited. Also, similar to the gene results, the extracellular secretion of TNF α (pro-inflammatory factor, Fig. 4C) decreased and IL-10 (Fig. 4D) increased proportionately with the increase of Sr²⁺ in MAO coatings [TNF α : comparison of Ti and Sr25%/Sr50% groups ($p < 0.05$), comparison of Ti/Sr0%/Sr25%/Sr50% and Sr75%/Sr100% groups ($p < 0.05$); IL-10: comparison of Ti/Sr0%/Sr25% and Sr75%/Sr100% groups ($p < 0.05$)].

In summary, the high proportion strontium-doped samples could effectively eliminate the OS-induced damages of macrophages and accelerate their M2 phenotype polarization, thus promoting early osseointegration of Ti-based implants.

3.4. The behaviors of MC3T3-E1 cells in macrophage conditioned medium

Because M2 macrophages have been reported to be conducive to osteoinduction, we further evaluated the osteogenic ability of MC3T3-E1 cells in different macrophage-conditioned medium. The cell viability, ALP activity, collagen expression, mineralization level, and osteogenic gene expression studies were conducted. Fig. 5B depicted that the MC3T3-E1 cells in the Sr100% group had the best viability (comparison of Ti and Sr100% groups: $p < 0.05$; comparison of Sr25%/Sr50% and Sr100% groups: $p < 0.05$), which was different from that in the independent culture (as shown in Fig. 3D: the S75% group was the best). No significant differences in cell viability were observed in the other five groups (Ti, Sr0%, Sr25%, Sr50% & Sr75%). The results of collagen secretion (Fig. 5D) presented a similar trend to the cell viability result. Although the amount of collagen secreted by MC3T3-E1 cells on Sr100% substrates was the highest, there were no significant differences among the Sr-incorporated groups apart from Ti group (comparison of Ti and Sr100% groups: $p < 0.05$). It was also observed that the ALP activity and mineralization level of MC3T3-E1 in Sr75% and Sr100% groups were significantly higher ($p < 0.05$) than those in Ti and/or Sr0% groups in the conditioned medium (Fig. 5C and E). The RT-qPCR analysis of Runx2, ALP, COL I, OPN and OCN gene expressions were significantly increased for both Sr100% (highest expression) and Sr75% groups [Fig. 5F; Runx2/COL I: comparison of Ti/Sr0%/Sr25% and Sr50%/Sr75% groups ($p < 0.05$); Runx2/COL I/OPN/OCN: comparison of Ti/Sr0%/Sr25%/Sr50%/Sr75% and Sr100% groups ($p < 0.05$); ALP: comparison of Ti/Sr0% and Sr75%/Sr100% groups ($p < 0.05$); OPN:

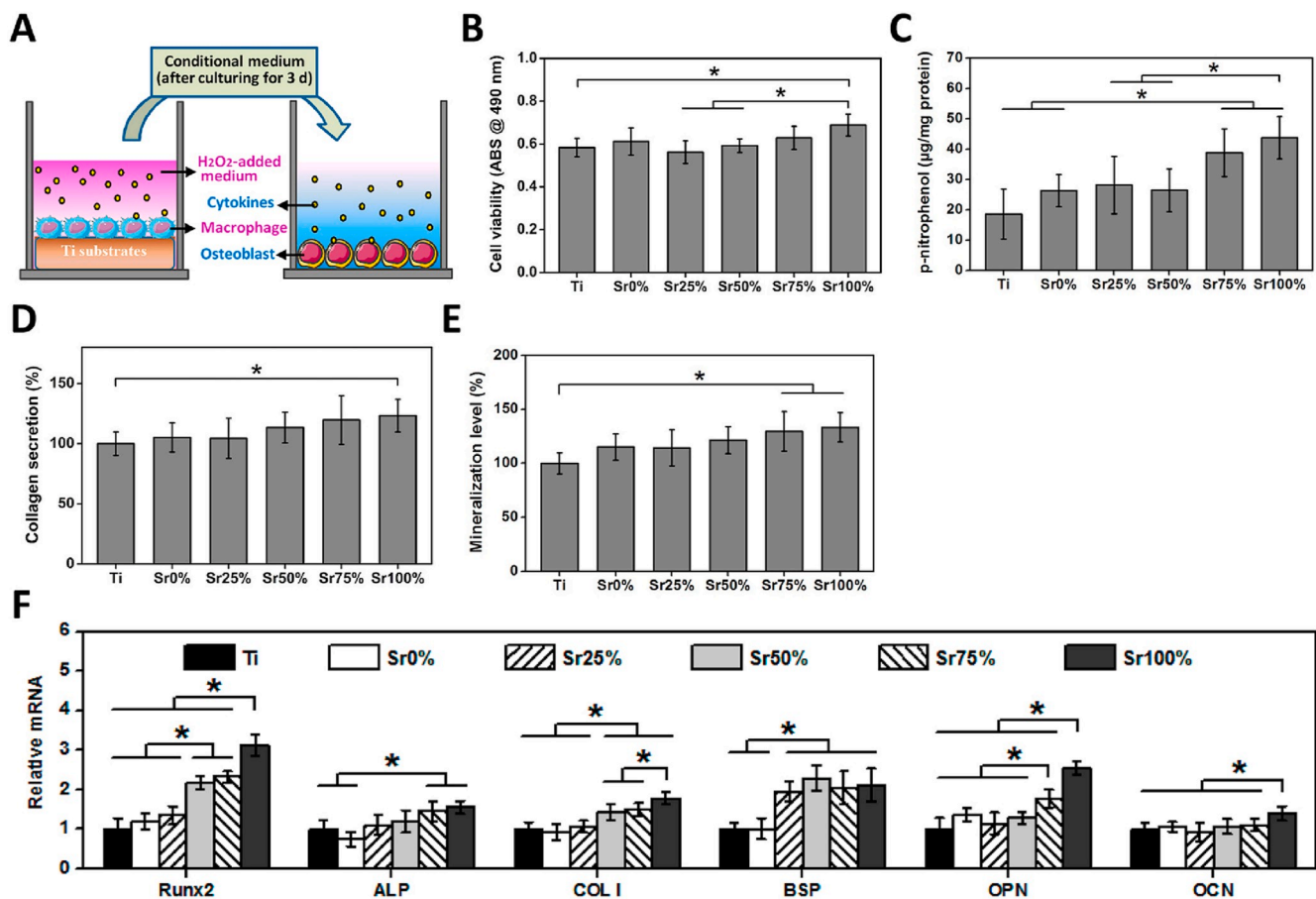


Fig. 5. Co-culture experiments with H₂O₂-stimulated RAW264.7 and MC3T3-E1 cells *in vitro*: (A) schematic diagram of cell co-culture process; quantitative statistics of cell viability (B), ALP activity (C), collagen secretion (D), and mineralization (E); (F) expression of osteogenesis-related genes in different groups. Error bars represent mean \pm SD for $n = 6$, * $p < 0.05$.

comparison of Ti/Sr0%/Sr25%/Sr50% and Sr75% groups ($p < 0.05$). For BSP, the gene expression of Sr25%, Sr50%, Sr75% and Sr100% groups were significantly higher ($p < 0.05$) than that of Ti and Sr0% groups, and no observable differences could be observed among the four groups.

With the collected data, we were able to determine that the cytokines (e.g., TGF β 1, BMP2, etc.) of RAW264.7 cells in Sr100% group could effectively promote the osteogenic differentiation of MC3T3-E1 cells, thus was the most conducive to osteogenesis. This was different from the optimal performance of Sr75% group in independent culture.

3.5. In vivo osseointegration

Based on the collected *in vitro* results, we were able to determine that the low and high Sr-doped samples were favorable for osteogenesis under normal and osteoporotic conditions, respectively. Thus, we had screened 4 groups for the following *in vivo* study: Ti, Sr0%, Sr25%, and Sr100% implants. To verify the success of fabricating an osteoporotic rat model, HE staining was first utilized to observe the presence of vacuoles, which could be seen in the bone tissue of ovariectomized rats, indicated with blue arrows (Fig. S8A).

Micro-CT was then utilized to observe the new bone formation around different implants in normal and osteoporotic rats and the results are displayed in Fig. S8B and Fig. 6. Three specific regions were selected to evaluate the osteogenesis in osteoporotic groups: epiphysis (E), epiphyseal line (EL), and diaphysis (D). The purple areas represented Ti-based implants, and the white tissue (blue arrows) around the implant

represented the new bone formation. From Fig. S8C, it was discovered that in normal rats, the new bone volume (BV/TV) and trabecular number (Tb.N) in Sr25% group were slightly better than those in Sr100% group, but there was no significant difference between the two groups. However, in the osteoporosis model, the Sr100% group showed a better bone-implant integration, with the most obvious new bone formation (Fig. 6A). Further quantitative data (Fig. 6B–E) also showed that new bone formation occurred around each group, but became more apparent with the increase of Sr doping. No significant difference could be observed between Ti and Sr0% groups for their BV/TV, Tb.N, Tb.Th and Tb.Sp results in the three regions (E, EL and D). In comparison to Ti and Sr0% groups, the Tb.N and Tb.Th of Sr25% [Tb.N (%): 121.9 \pm 8.0 (E), 133.9 \pm 9.1 (EL), 103.1 \pm 6.5 (D); Tb.Th (%): 138.8 \pm 16.9 (E), 161.9 \pm 7.4 (EL), 132.3 \pm 8.2 (D)] and Sr100% [Tb.N (%):139.2 \pm 5.2 (E), 149.7 \pm 4.9 (EL), 122.4 \pm 7.9 (D); Tb.Th (%): 171.2 \pm 12.1 (E), 179.6 \pm 8.5 (EL), 156.1 \pm 8.4 (D)] increased significantly ($p < 0.05$), in which the latter group has the most increase. In addition, the BV/TV (%) [9.3 \pm 1.0 (E), 10.8 \pm 1.5 (EL), 7.3 \pm 0.5 (D)] was significantly higher ($p < 0.05$) and the Tb.Sp (%) [72.0 \pm 4.0 (E), 72.1 \pm 3.4 (EL), 86.8 \pm 3.3 (D)] was significantly lower ($p < 0.05$) in Sr100% group when compared to the other three groups.

We had utilized both HE and Masson trichrome staining to further analyze the formation of new bone around different implants. The HE staining images (Fig. 7A) showed that a thicker new bone tissue (black arrows) around the Sr-doped implants were formed (Sr25% & Sr100%, especially the latter) in the E, EL and D regions. The contact area of Sr25% and Sr100% with the new bone were also significantly increased

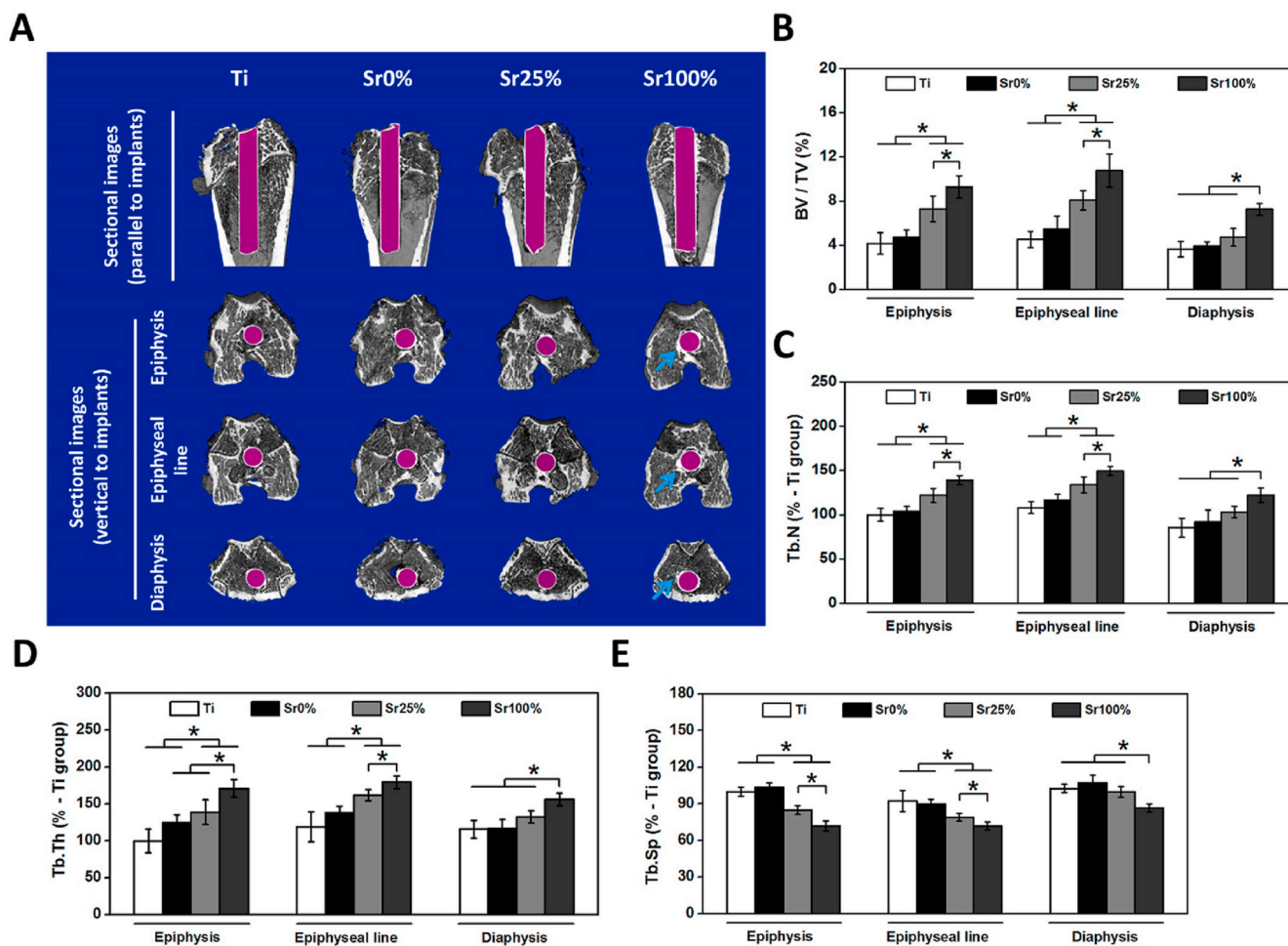


Fig. 6. Investigation of osteogenesis in osteoporotic rats: (A) representative micro-CT scan images of different groups; quantitative statistics of BV/TV (B), Tb.N (C), Tb.Th (D) and Tb.Sp (E) according to the above micro-CT images. Error bars represent mean \pm SD for $n = 10$, * $p < 0.05$.

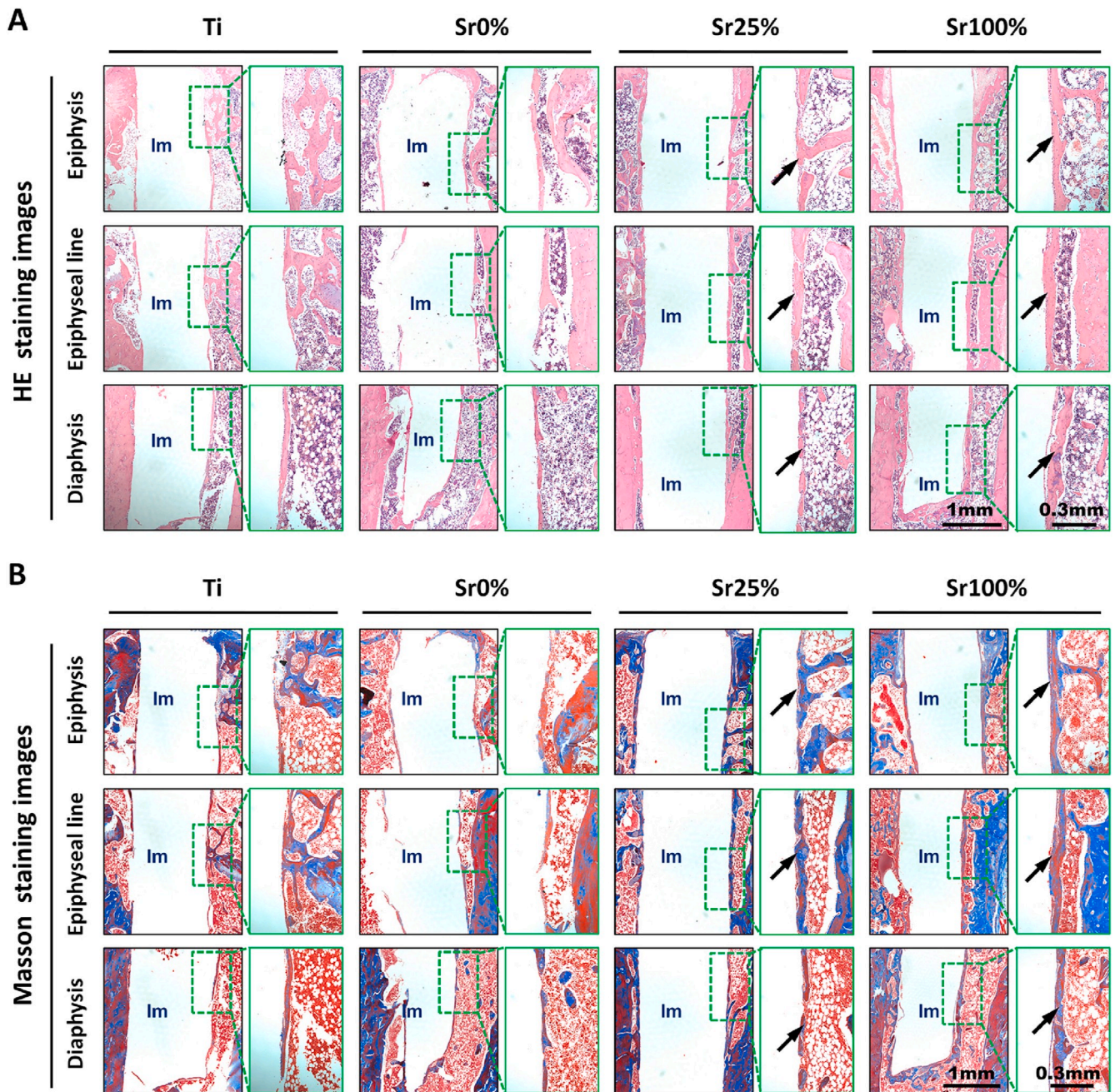


Fig. 7. Evaluation of new bone mass and maturity *in vivo*: (A) representative HE staining images of bone tissue (BT) around different implants (Im) in epiphysis, epiphyseal line and diaphysis regions; (B) representative Masson staining images of new bone maturity at different sites. The blue and red represent low and high maturity bone tissue, respectively.

compared with the control group. Next, similar results were observed in Masson trichrome staining images (Fig. 7B). More new bone formation (black arrows) could be also observed in the Sr25% and Sr100% groups. Due to the gradual colour change of the Masson trichrome stain as bone matures (from blue to red), we came to a conclusion that compared to the new bone formation of Sr25% group, the newly formed bone of Sr100% group was more mature. Overall, Sr100% implants not only promoted the formation of new bone, but also had a positive effect on its maturation.

To study the phenotypes of macrophages around different implants *in vivo*, CD68 (red, monocyte maker), Arg (green, M2 macrophage maker) and iNOS (green, M1 macrophage maker) were detected by immunofluorescence staining. As depicted in Fig. 8A, the fluorescence intensity of Arg increased correspondingly with higher Sr accumulation

and showed that the highest intensity appeared in Sr100% group (comparison of Ti/Sr0% and Sr25%/Sr100% groups: $p < 0.05$; comparison of Sr25% and Sr100% groups: $p < 0.05$). In contrast, the fluorescent staining intensity of iNOS was opposite to that of Arg, where it decreased with the increase of Sr in the coatings (Fig. 8B; comparison of Ti/Sr0% and Sr25%/Sr100% groups: $p < 0.05$). Further quantitative analysis (Fig. 8C) also showed that when compared to Ti group, the Arg intensity of Sr75% and Sr100% increased to 129% and 152%, while iNOS decreased to 76% and 73%, respectively. The Arg/iNOS ratio, which was often used to assess macrophage phenotypes, was also significantly higher ($p < 0.05$) in the Sr75% and Sr100% groups, increasing to about 170% and 203%, respectively.

In addition, DHE staining was further utilized to detect the level of ROS and its effect on different implants *in vivo*. The intensity of red

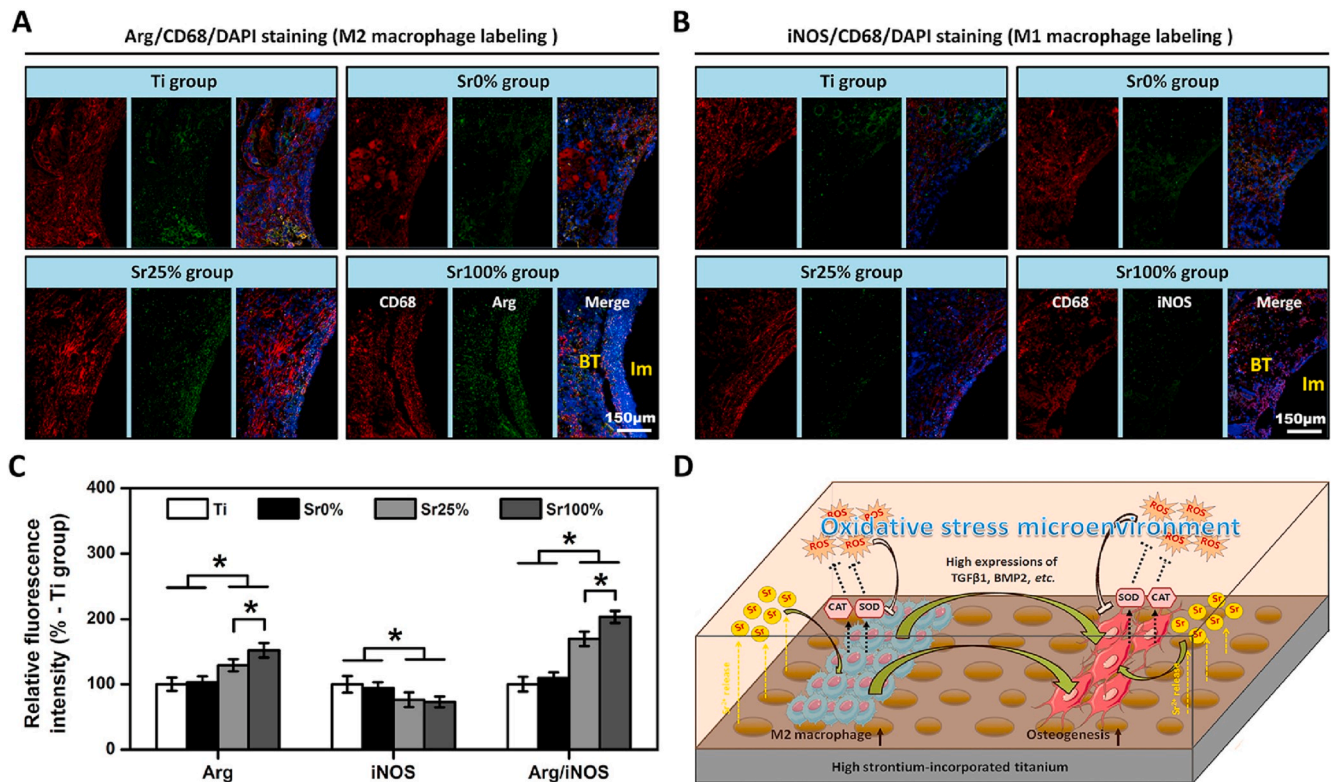


Fig. 8. Polarization characterization of macrophages *in vivo*: representative immunofluorescence staining images of Arg/CD68/DAPI (A) and iNOS/CD68/DAPI (B) after implantation for 7 d (BT: bone tissue; Im: implants); (C) the relative fluorescence intensities of Arg, iNOS and Arg/iNOS according to the above fluorescent images. Error bars represent mean \pm SD for $n = 8$, * $p < 0.05$; (D) schematic diagram of high Sr-incorporated samples inhibiting ROS injury and promoting new bone formation under OS conditions.

fluorescence represented the expression of ROS in living tissues. As shown in Fig. S9, the fluorescence intensity gradually darkened with the increase of Sr content. The corresponding data further confirmed that the intensity in Sr100% group was the lowest (comparison of Ti/Sr0% and Sr25%/Sr100% groups: $p < 0.05$; comparison of Sr25% and Sr100% groups: $p < 0.05$), which suggested that high concentration of Sr^{2+} had an excellent effect on decreasing the expression of ROS in osteoporosis. In conclusion, the results of immunofluorescence staining were consistent with those of cell culture *in vitro*, and high Sr-doped calcium phosphate coatings could effectively promote the formation of more M2 macrophages and decrease ROS expression.

4. Discussion

Reports have claimed that the bioactivities of biomaterials are closely correlated to their surface physicochemical properties (e.g., roughness, wettability, crystal structure, etc.) [29,31,32]. Consequentially, surface modifications have been widely utilized in the recent decade in order to improve the osteoinductive capacity of Ti-based materials. By studying osteoclast activity on titanium surfaces with varying surface roughness, Zhang et al. revealed that the different roughness would influence osteoclastogenesis [33]. Another study conducted by Hotchkiss et al. demonstrated a significant augmentation in the activation of macrophage anti-inflammatory properties by regulating the surface morphology and wettability of titanium, thus creating a microenvironment that could potentially reduce healing time and enhance osseointegration [34]. In our study, a series of Sr-doped titanium surface coatings (Sr0%, Sr25%, Sr50%, Sr75% and Sr100%) were successfully fabricated through MAO. The changes in the ratio of Sr and Ca doping were depicted to be the only variable in regards to the physicochemical properties of the sample surfaces (Figs. 1–2 & Fig. S1–S3). This made it possible to further investigate the effects of the

different proportions of Sr^{2+} under normal and OS conditions.

As one of the most commonly used surface modification techniques, MAO treatment creates a porous oxide layer on the surface of Ti with superior bonding strength to enhance biocompatibility [35]. The process involved in MAO is not only limited to the production of hydrogen and oxygen at the cathode and anode, respectively, but also the deposition of oxide compounds on the surface of the anode metal [16,17,36]. Yerokhin et al. demonstrated that, when a direct electric current was passed through, H^+ and a part of Cation^{n+} in the electrolyte would migrate to the cathode and undergo reduction to form H_2 and Cation^0 [37]. In contrast, the oxidation of both O^{2-} and anode Metal^0 would form O_2 and Metal^{n+} at the surface of the anode. Furthermore, a portion of Cation^{n+} and Metal^{n+} in the electrolyte will be combined with O^{2-} to form a relative oxide layer on the surface of the anode metal [37]. In our study, the XPS results (Fig. 2A–D) showed that the MAO coatings consisted of CaO/SrO , $(\text{Ca/Sr})_3(\text{PO}_4)_2$, $(\text{Ca/Sr})\text{TiO}_3$, and TiO_2 compounds. The observed ratio of $\text{Sr}/(\text{Ca} + \text{Sr})$ was lower than its theoretical value (Fig. 1B), indicating that the deposition of Ca^{2+} on the coatings was greater than its theoretical value. Because Cation^{n+} was replenished by diffusion after being reduced by deposition near the anode metal, the diffusion rates of the various Cation^{n+} were proportional to their concentration in the produced MAO coatings. The atomic radius of Sr is much larger than that of Ca, which makes the diffusion rate of Sr^{2+} in the electrolyte relatively slow [38,39]. This may be the main reason for the higher Ca^{2+} content in the coating than the theoretical value.

In-depth evaluation of the composition of Sr compounds in the coatings showed that the ratio of SrTiO_3 remained unchanged while $\text{Sr}_3(\text{PO}_4)_2$ decreased and SrO increased gradually with the increase in Sr proportion. We speculated that Ti was firstly oxidized into Ti^{4+} by high voltage, which then combined with O^{2-} resulting in the formation of TiO_3^{2-} , and then followed by its reaction with the free Sr^{2+} in the electrolyte to form SrTiO_3 on the surface of titanium pieces [40,41].

Because PO_4^{3-} had a certain rate of migration, the consumed PO_4^{3-} that reacted with Sr^{2+} and Ca^{2+} could not be supplemented in time, which led to the reduction of local PO_4^{3-} concentration. In addition, Sr^{2+} that had not reacted with PO_4^{3-} , combined with O^{2-} to form SrO and were deposited on the surface of titanium. This resulted in an increase of SrO proportions, which corresponded to an increase of Sr^{2+} . The enhanced SrO component in the high Sr coatings would easily react with water to generate $\text{Sr}(\text{OH})_2$ and subsequently dissolve in aqueous solution [42], resulting in a greater release rate of Sr^{2+} in the Sr100% group than in the Sr25% group, as demonstrated in our work (Fig. S4).

Previously reported study has also claimed that Sr is readily incorporable with anions to form various compounds such as $\text{Sr}_3(\text{PO}_4)_2$ and SrO during the MAO process [43]. These Sr-contained compounds will then progressively degrade, releasing Sr^{2+} into the surrounding environment, thereby promoting osteogenesis and inhibiting osteolysis [44]. The *in vitro* studies (Fig. S5) verified that an appropriate amount of Sr doping was advantageous for cellular bioactivity under normal conditions, demonstrating that the high Sr samples (particularly Sr75% and Sr100%) had similar bioactivity to the control (Ti) group, but had some cytotoxicity compared with the Sr25% group. In concurrence with previously reported studies, the exploitation of Sr for its osteogenic properties was highly dose-dependent [26,27,36]. However, in contrast to the results obtained for the normal microenvironment, high dose Sr-doped samples (Sr75% and Sr100%) exhibited good osteogenic properties under the OS microenvironment (Figs. 3–7). This could be correlated to the up-regulation of the antioxidant system by high dose Sr^{2+} on osteoblasts/macrophages, thus effectively eliminated the excessive accumulation of endogenous ROS. Furthermore, coupled with the findings of the *in vivo* implantation procedures in normal and osteoporotic rats, we confirmed that the high Sr-doped samples had no detrimental impacts on the development of the surrounding new bone. As a result, we considered that all of the Sr-doped specimens prepared in this study were biologically safe enough for potential clinical uses.

Results of a previous study also showed that Ca^{2+} had a concentration-dependent osteoinductivity [45]. It was demonstrated that when the optimum concentration range was determined, osteogenesis would be enhanced when Ca^{2+} increased within the range (1–16 mM) [45]. Surpassing this limit, however, would result in cytotoxicity. According to the *in vitro* cell findings, the Sr0% specimens with the greatest Ca^{2+} concentration exhibited no observable cytotoxicity to MC3T3-E1 cells under both normal and OS conditions (Fig. S5A & 3D). This indicated that the Ca^{2+} released from all the MAO-treated samples did not surpass the maximum tolerance limit of the MC3T3-E1 cells. As a result, the decrease in Ca^{2+} in the high Sr-doped samples could not have contributed to their improved osteogenesis properties. Furthermore, no substantial antioxidant activities of Ca^{2+} have been demonstrated in previous studies. Therefore, we believed that the superior capacities of osteoinduction and anti-oxidation in high Sr-doped groups under OS conditions were mainly due to the slow release of Sr^{2+} rather than Ca^{2+} .

As is known, the excessive accumulation of ROS is detrimental to bone homeostasis, ultimately causing osteocyte apoptosis and bone loss [46]. Consequentially, studies regarding anti-oxidative stress have garnered widespread attention in recent years. The mechanisms of anti-oxidative stress had been partially summarized as follows: 1) inhibiting the formation of free radicals (representative antioxidants: SOD, CAT, Cu, etc.); 2) elimination of free radicals to mitigate subsequent adverse effects (representative antioxidants: vitamin C, vitamin E, etc.); 3) repairing free radicals-induced damages (representative antioxidants: lipases, proteases, etc.) [47]. Qi et al. used strontium fructose 1,6-diphosphate (FDP-Sr) to further show the anti-oxidative stress mechanism of Sr, demonstrating its efficacy through the inhibition of osteoblast apoptosis by inducing caspase 3 to reduce ROS production [48]. In our study, we discovered that the anti-oxidative stress property of both MC3T3-E1 and RAW264.7 cells was significantly improved in high Sr groups under OS microenvironment (Fig. 3A & S7A). To elucidate this phenomenon, we detected the activity of CAT/SOD and found

that both showed significant improvement in response to high doses of Sr (Fig. 3B & S7B). SOD enzyme has been shown to expedite the process that converts $\cdot\text{O}_2^-$ into H_2O_2 , whereas CAT enzyme catalyzes the transformation of H_2O_2 into H_2O and O_2 [49,50]. Therefore, we can conclude that the anti-oxidative stress capability of high Sr-doped samples (Sr75% and Sr100%) was improved due to the increased activity of CAT and SOD in the OS microenvironment.

Another critical issue to consider is the interaction between the biomaterial and the host's immune system. According to previous studies, osteoimmunomodulation has become more widely acknowledged as an essential component in bone regeneration because it effectively regulates the bone immune environment to promote bone tissue regeneration [51,52]. Also, it is shown that ROS acts as both the signaling and effector molecules during an inflammatory response, resulting in the recruitment of immune cells to the implant site which could interfere with osseointegration as well as cause damage and fibrosis to the surrounding tissues [53,54]. In addition, because of their capacity to be stimulated to develop into osteoclasts, close correlation to osteo-immunomodulation, and the heterogeneity of M1/M2 polarization, macrophages have attracted a great deal of attention [55–57]. As for osteogenesis, M2 macrophage could significantly stimulate mesenchymal stem cells (MSCs)/precursor osteoblast cells to differentiate into mature osteoblasts and enhance bone mineralization, which was ascribed in part to M2 macrophages secreting anti-inflammatory factors (e.g., IL-4, IL-10, etc.) and growth factors (e.g., BMP2, TGF β , etc.) [58, 59]. In angiogenesis, factors secreted from M2 macrophage, especially platelet-derived growth factor-BB (PDGF-BB), could effectively promote the formation of new blood vessels, thus accelerating the process of bone repair [60]. Furthermore, in the prevention of osteolysis, M2 cytokines such as IL-4 and IL-13 could inhibit bone resorption by inhibiting not only the differentiation of osteoclast precursors but also the activities of mature osteoclasts [61]. As a result, M2 macrophages play a pivotal role in facilitating osteogenesis/angiogenesis and inhibiting osteolysis, which has considerable theoretical and practical importance in improving the bone health of patients with osteoporosis. In our study, we found that the macrophages in the high Sr groups (especially Sr100%) exhibited larger cell surface area and more pseudopodia (Fig. 4A), which was similar to the cell morphology of M2 macrophage described by Kazimierzak et al. [62]. This further confirms that the high Sr specimens significantly increase the polarization of macrophages from M0 to M2 as well as the expression of the various anti-inflammatory genes/factors (IL10 & IL1ra; Fig. 4B–D). We also found a decrease in the expression of pro-inflammatory genes/factors (TNF α & IL6) under OS conditions. In addition, the overexpression of BMP2 and TGF β 1 could be observed, further verifying that M2 macrophages promoted the osteogenic differentiation of MC3T3-E1 cells (Fig. 5). This was consistent with the findings of Chen et al. that the antioxidant Ag@TiO $_2$ -NTs could effectively enhance the M2 polarization of macrophages by eliminating ROS, therefore providing a favorable microenvironment to regulate osteoimmunomodulatory activities [63].

Having proven the efficacy of the antioxidative as well as the osteogenesis properties of Sr-doped Ti implants *in vitro*, we further investigated the osseointegration capacity of said implants through *in vivo* studies. In this study, we have subjected the rats to bilateral ovariectomy (OVX), which was consistent with a previous study and could simulate the high OS microenvironment in osteoporotic patients [30]. All of the micro-CT, HE, and Masson's staining results (Figs. 6 and 7) proved that Sr100% implants were the most conducive to osteogenesis. From the immunofluorescence observations (Fig. 8A–C), we also discovered that the M2 biomarker (Arg) was significantly increased, while the M1 biomarker (iNOS) decreased in the Sr100% group. This indicated an increase in the number of M2 macrophages. Furthermore, when compared with both Ti and low Sr groups, the DHE observations (Fig. S9) revealed a significant decrease in the ROS expression of the Sr100% group. Ultimately, the collated data verified that the high

proportion of Sr doping (Sr100%) could promote osteogenesis, induce M2 polarization of macrophages, and decrease ROS level in the surrounding bone tissue, which was in line with our *in vitro* results.

In conclusion, the high Sr samples could regulate both osteoblasts and macrophages in an osteoporosis-induced high OS microenvironment by releasing high doses of Sr²⁺, facilitating the early osseointegration of implants. The mechanisms (Fig. 8D) involved are summarized as follows: 1) the released Sr²⁺ enhances the antioxidative enzyme (CAT & SOD) activity to eliminate excessive endogenous ROS of osteoblasts, endowing superior osteoinduction and anti-oxidative properties of Sr75% and Sr100% samples; 2) Sr²⁺ influences both the cellular structure and the CAT/SOD activity of macrophages by inhibiting the production of OS and the inflammation levels, thereby promoting the polarization of M0 macrophages into M2; 3) the overexpression of osteogenic-related cytokines, such as TGFβ1, BMP2 by M2 macrophages could ameliorate osteogenesis. Although we were able to sufficiently demonstrate the functional differences between high and low Sr-doped samples in normal and osteoporotic models, the following limitations remain to be addressed: 1) there has been inadequate research into the mechanisms of anti-oxidative stress and osteoimmunomodulation in high Sr groups; 2) it is unclear if patients with osteoporosis should choose various proportions of Sr-doped implants depending on the severity of the illness. Having said that, we will perform comprehensive research in the future to investigate the functions and potential mechanisms between different OS levels and Sr-doped implants, which will be critical for patients with varying degrees of osteoporosis in order to select the most appropriate Sr-doped implants.

5. Conclusion

In this study, we have successfully fabricated an MAO-assisted titanium coating consisting of varying proportions of Sr and Ca ions. We discovered that when the initial Sr²⁺ concentration in the electrolyte increased, the ratio of Sr compounds (particularly SrO) on the target coating increased significantly. This resulted in the large release of Sr²⁺ from the high Sr samples (Sr75% or Sr100%) at the early stage, which led to the cytotoxicity of MC3T3-E1 cells under normal conditions. In contrast, the aforementioned effects facilitated the cellular bioactivity under OS, showing excellent cell viability, anti-oxidation, anti-inflammation, and osteogenesis properties of Sr75% and/or Sr100% groups. This was attributable to the up-regulation of CAT/SOD enzyme activity, causing the elimination of excess ROS. Furthermore, the high Sr coatings significantly enhanced the M2 polarization of macrophages and the expression of multiple osteogenesis-related factors (TGFβ1 & BMP2), and were favorable to osteoimmunomodulation. We believe that the fabrication of a high proportion Sr-doped Ti coatings utilizing MAO, notably the Sr100% group, holds a promising theoretical and practical significance for the future development of ion-doped implants equipped with antioxidative properties to promote the early osseointegration of implants in patients with osteoporosis.

Data availability statement

The datasets generated for this study are available on request to the corresponding author.

CRediT authorship contribution statement

Xinkun Shen: Data curation, Formal analysis, Writing – original draft, preparation. **Kai Fang:** Data curation, Formal analysis, Writing – original draft, preparation. **Kendrick Hii Ru Yie:** Methodology, Software. **Zixin Zhou:** Visualization, Investigation. **Yiding Shen:** Methodology, Software. **Shuyi Wu:** Visualization, Investigation. **Yue Zhu:** Software, Validation. **Zhennan Deng:** Software, Validation. **Pingping Ma:** Conceptualization, Writing – review & editing. **Jianfeng Ma:** Supervision. **Jinsong Liu:** Conceptualization, Writing – review & editing.

Declaration of competing interest

We have no conflicts of interest to declare.

Acknowledgments

This work was funded by National Natural Science Foundation of China (82171004, 82071170 & 81701016), Zhejiang Provincial Science and Technology Project for Public Welfare (LY21H180006 & LGF20H140002), Key Technological Innovation Projects of Wenzhou (ZY2019009), Wenzhou Public Welfare Science and Technology Project (Y20190099 & Y2020118), Wenzhou Medical University Basic Scientific Research Operating Expenses (KYYW201905).

Appendix A. Supplementary data

Supplementary data to this article can be found online at <https://doi.org/10.1016/j.bioactmat.2021.08.031>.

References

- [1] J.N. Oliver, Y. Su, X. Lu, P.H. Kuo, J. Du, D. Zhu, Bioactive glass coatings on metallic implants for biomedical applications, *Bioact. Mater.* 4 (2019) 261–270, <https://doi.org/10.1016/j.bioactmat.2019.09.002>.
- [2] S. Ray, U. Thormann, M. Eichelroth, M. Budak, C. Biehl, M. Rupp, U. Sommer, T. El Khassawna, F.I. Alagboso, M. Kampschulte, M. Rohnke, A. Henß, K. Peppeler, V. Linke, P. Quadbeck, A. Voigt, F. Stenger, D. Karl, R. Schnettler, C. Heiss, K. S. Lips, V. Alt, Strontium and bisphosphonate coated iron foam scaffolds for osteoporotic fracture defect healing, *Biomaterials* 157 (2018) 1–16, <https://doi.org/10.1016/j.biomaterials.2017.11.049>.
- [3] T.L. Yang, H. Shen, A. Liu, S.S. Dong, L. Zhang, F.Y. Deng, Q. Zhao, H.W. Deng, A road map for understanding molecular and genetic determinants of osteoporosis, *Nat. Rev. Endocrinol.* 16 (2020) 91–103, <https://doi.org/10.1038/s41574-019-0282-7>.
- [4] M. Arioka, X. Zhang, Z. Li, U.S. Tulu, Y. Liu, L. Wang, X. Yuan, J.A. Helms, Osteoporotic changes in the periodontium impair alveolar bone healing, *J. Dent. Res.* 98 (2019) 450–458, <https://doi.org/10.1177/0022034518818456>.
- [5] X. Cheng, K. Zhao, X. Zha, X. Du, Y. Li, S. Chen, Y. Wu, S. Li, Y. Lu, Y. Zhang, X. Xiao, Y. Li, X. Ma, X. Gong, W. Chen, Y. Yang, J. Jiao, B. Chen, Y. Lv, J. Gao, G. Hong, Y. Pan, Y. Yan, H. Qi, L. Ran, J. Zhai, L. Wang, K. Li, H. Fu, J. Wu, S. Liu, G.M. Blake, P.J. Pickhardt, Y. Ma, X. Fu, S. Dong, Q. Zeng, Z. Guo, K. Hind, K. Engelke, W. Tian, China Health Big Data (China Biobank) project investigators, Opportunistic screening using low-dose CT and the prevalence of osteoporosis in China: a nationwide, multicenter study, *J. Bone Miner. Res.* 36 (2021) 427–435, <https://doi.org/10.1002/jbmr.4187>.
- [6] Y. Hu, X. Chen, S. Wang, Y. Jing, J. Su, Subchondral bone microenvironment in osteoarthritis and pain, *Bone Res.* 9 (2021) 20, <https://doi.org/10.1038/s41413-021-00147-z>.
- [7] B. Yu, C.Y. Wang, Osteoporosis, a result of an “aged” bone microenvironment, *Trends Mol. Med.* 22 (2016) 641–644, <https://doi.org/10.1016/j.molmed.2016.06.002>.
- [8] S.C. Manolagas, From estrogen-centric to aging and oxidative stress: a revised perspective of the pathogenesis of osteoporosis, *Endocr. Rev.* 31 (2010) 266–300, <https://doi.org/10.1210/er.2009-0024>.
- [9] V. Domazetovic, G. Marcucci, T. Iantomasi, M.L. Brandi, M.T. Vincenzini, Oxidative stress in bone remodeling: role of antioxidants, *Clin. Cases Miner. Bone Metab.* 14 (2017) 209–216, <https://doi.org/10.11138/ccmbm/2017.14.1.209>.
- [10] D. Shao, K. Li, T. Hu, S. Wang, X. Zheng, Titania nanotube array supported nanoceria with redox cycling stability ameliorates oxidative stress-inhibited osteogenesis, *Chem. Eng. J.* 415 (2021) 128913, <https://doi.org/10.1016/j.cej.2021.128913>.
- [11] Y. Huang, Z. Du, P. Wei, F. Chen, X. Yang, Biodegradable microspheres made of conductive polyorganophosphazene showing antioxidant capacity for improved bone regeneration, *Chem. Eng. J.* 397 (2020) 125352, <https://doi.org/10.1016/j.cej.2020.125352>.
- [12] M. Iwai-Yoshida, Y. Shibata, Wurihan, D. Suzuki, N. Fujisawa, Y. Tanimoto, R. Kamijo, K. Maki, T. Miyazaki, Antioxidant and osteogenic properties of anodically oxidized titanium, *J. Mech. Behav. Biomed. Mater.* 13 (2012) 230–236, <https://doi.org/10.1016/j.jmbbm.2012.01.016>.
- [13] Y. Yu, X. Shen, Z. Luo, Y. Hu, M. Li, P. Ma, Q. Ran, L. Dai, Y. He, K. Cai, Osteogenesis potential of different titania nanotubes in oxidative stress microenvironment, *Biomaterials* 167 (2018) 44–57, <https://doi.org/10.1016/j.biomaterials.2018.03.024>.
- [14] X.Y. Ma, T.C. Ma, Y.F. Feng, G. Xiang, W. Lei, D.P. Zhou, H.L. Yu, L.B. Xiang, L. Wang, Promotion of osteointegration by silk fibroin coating under diabetic conditions on 3D printed porous titanium implants via ROS-mediated NF-κB pathway, *Biomed. Mater.* 16 (2020), 035015, <https://doi.org/10.1088/1748-605X/abaa1>.
- [15] T. Tenkumo, A. Aobulikasimu, Y. Asou, M. Shirato, S. Shishido, T. Kanno, Y. Niwano, K. Sasaki, K. Nakamura, Proanthocyanidin-rich grape seed extract

- improves bone loss, bone healing, and implant osseointegration in ovariectomized animals, *Sci. Rep.* 10 (2020) 8812, <https://doi.org/10.1038/s41598-020-65403-4>.
- [16] Q. Du, D. Wei, Y. Wang, S. Cheng, S. Liu, Y. Zhou, D. Jia, The effect of applied voltages on the structure, apatite-inducing ability and antibacterial ability of micro arc oxidation coating formed on titanium surface, *Bioact. Mater.* 3 (2018) 426–433, <https://doi.org/10.1016/j.bioactmat.2018.06.001>.
- [17] B. Zhao, X. Li, H. Xu, Y. Jiang, D. Wang, R. Liu, Influence of simvastatin-strontium-hydroxyapatite coated implant formed by micro-arc oxidation and immersion method on osteointegration in osteoporotic rabbits, *Int. J. Nanomed.* 15 (2020) 1797–1807, <https://doi.org/10.2147/IJN.S244815>.
- [18] J. Li, C. Deng, W. Liang, F. Kang, Y. Bai, B. Ma, C. Wu, S. Dong, Mn-containing bioceramics inhibit osteoclastogenesis and promote osteoporotic bone regeneration via scavenging ROS, *Bioact. Mater.* 6 (2021) 3839–3850, <https://doi.org/10.1016/j.bioactmat.2021.03.039>.
- [19] J. Duan, Z. Chen, X. Liang, Y. Chen, H. Li, X. Tian, M. Zhang, X. Wang, H. Sun, D. Kong, Y. Li, J. Yang, Construction and application of therapeutic metal-polyphenol capsule for peripheral artery disease, *Biomaterials* 255 (2020) 120199, <https://doi.org/10.1016/j.biomaterials.2020.120199>.
- [20] S. Jebahi, H. Oudadesse, N. Jarda, I. Khayat, H. Keskes, A. Khabir, T. Rebai, H. El Feki, A. El Feki, Biological therapy of strontium-substituted bioglass for soft tissue wound-healing: responses to oxidative stress in ovariectomized rats, *Ann. Pharm. Fr.* 71 (2013) 234–242, <https://doi.org/10.1016/j.pharma.2013.05.003>.
- [21] K. Xu, W. Chen, Y. Hu, X. Shen, G. Xu, Q. Ran, Y. Yu, C. Mu, K. Cai, Influence of strontium ions incorporated into nanosheet-pore topographical titanium substrates on osteogenic differentiation of mesenchymal stem cells *in vitro* and on osseointegration *in vivo*, *J. Mater. Chem. B* 4 (2016) 4549–4564, <https://doi.org/10.1039/c6tb00724d>.
- [22] W. Lu, Y. Zhou, H. Yang, Z. Cheng, F. He, Efficacy of strontium supplementation on implant osseointegration under osteoporotic conditions: a systematic review, *J. Prosthet. Dent.* (2021), <https://doi.org/10.1016/j.prosdent.2020.12.031> doi: 10.1016/j.prosdent.2020.12.031.
- [23] M. Li, P. Wan, W. Wang, K. Yang, Y. Zhang, Y. Han, Regulation of osteogenesis and osteoclastogenesis by zoledronic acid loaded on biodegradable magnesium-strontium alloy, *Sci. Rep.* 9 (2019) 933, <https://doi.org/10.1038/s41598-018-37091-8>.
- [24] A.H. Lourenço, A.L. Torres, D.P. Vasconcelos, C. Ribeiro-Machado, J.N. Barbosa, M.A. Barbosa, C.C. Barrias, C.C. Ribeiro, Osteogenic, anti-osteoclastogenic and immunomodulatory properties of a strontium-releasing hybrid scaffold for bone repair, *Mater. Sci. Eng. C Mater. Biol. Appl.* 99 (2019) 1289–1303, <https://doi.org/10.1016/j.msec.2019.02.053>.
- [25] C. Zhou, Y.Q. Chen, Y.H. Zhu, G.F. Lin, L.F. Zhang, X.C. Liu, F.M. He, Antiadipogenesis and osseointegration of strontium-doped implant surfaces, *J. Dent. Res.* 98 (2019) 795–802, <https://doi.org/10.1177/0022034519850574>.
- [26] Y.Z. Huang, C.G. Wu, H.Q. Xie, Z.Y. Li, A. Silini, O. Parolini, Y. Wu, L. Deng, Y. C. Huang, Strontium promotes the proliferation and osteogenic differentiation of human placental decidual basalis- and bone marrow-derived MSCs in a dose-dependent manner, *Stem Cell. Int.* 2019 (2019) 4242178, <https://doi.org/10.1155/2019/4242178>.
- [27] A. Aimaity, A. Maimaitiyming, X. Boyong, K. Aji, C. Li, L. Cui, Low-dose strontium stimulates osteogenesis but high-dose doses cause apoptosis in human adipose-derived stem cells via regulation of the ERK1/2 signaling pathway, *Stem Cell Res. Ther.* 8 (2017) 282, <https://doi.org/10.1186/s13287-017-0726-8>.
- [28] J. Yan, J.F. Sun, P.K. Chu, Y. Han, Y.M. Zhang, Bone integration capability of a series of strontium-containing hydroxyapatite coatings formed by micro-arc oxidation, *J. Biomed. Mater. Res. A* 101 (2013) 2465–2480, <https://doi.org/10.1002/jbm.a.34548>.
- [29] W. Chen, X. Shen, Y. Hu, K. Xu, Q. Ran, Y. Yu, L. Dai, Z. Yuan, L. Huang, T. Shen, K. Cai, Surface functionalization of titanium implants with chitosan-catechol conjugate for suppression of ROS-induced cells damage and improvement of osteogenesis, *Biomaterials* 114 (2017) 82–96, <https://doi.org/10.1016/j.biomaterials.2016.10.055>.
- [30] K. Chen, P. Qiu, Y. Yuan, L. Zheng, J. He, C. Wang, Q. Guo, J. Kenny, Q. Liu, J. Zhao, J. Chen, J. Tickner, S. Fan, X. Lin, J. Xu, Pseurotin A inhibits osteoclastogenesis and prevents ovariectomized-induced bone loss by suppressing reactive oxygen species, *Theranostics* 9 (2019) 1634–1650, <https://doi.org/10.7150/thno.30206>.
- [31] Q. Wang, Y. Huang, Z. Qian, Nanostructured surface modification to bone implants for bone regeneration, *J. Biomed. Nanotechnol.* 14 (2018) 628–648, <https://doi.org/10.1166/jbn.2018.2516>.
- [32] Y. Deng, X. Liu, A. Xu, L. Wang, Z. Luo, Y. Zheng, F. Deng, J. Wei, Z. Tang, S. Wei, Effect of surface roughness on osteogenesis *in vitro* and osseointegration *in vivo* of carbon fiber-reinforced polyetheretherketone-nanohydroxyapatite composite, *Int. J. Nanomed.* 10 (2015) 1425–1447, <https://doi.org/10.2147/IJN.S75557>.
- [33] Y. Zhang, S.E. Chen, J. Shao, J.J.P. van den Beucken, Combinatorial surface roughness effects on osteoclastogenesis and osteogenesis, *ACS. Appl. Mater. Interfaces* 10 (2018) 36652–36663, <https://doi.org/10.1021/acsami.8b10992>.
- [34] K.M. Hotchkiss, G.B. Reddy, S.L. Hyzy, Z. Schwartz, B.D. Boyan, R. Olivares-Navarrete, Titanium surface characteristics, including topography and wettability, alter macrophage activation, *Acta Biomater.* 31 (2016) 425–434, <https://doi.org/10.1016/j.actbio.2015.12.003>.
- [35] L. Bai, Z. Du, J. Du, W. Yao, J. Zhang, Z. Weng, S. Liu, Y. Zhao, Y. Liu, X. Zhang, X. Huang, X. Yao, R. Crawford, R. Hang, D. Huang, B. Tang, Y. Xiao, A multifaceted coating on titanium dictates osteoimmunomodulation and osteo/angiogenesis towards ameliorative osseointegration, *Biomaterials* 162 (2018) 154–169, <https://doi.org/10.1016/j.biomaterials.2018.02.010>.
- [36] X. Guo, S. Wei, M. Lu, Z. Shao, J. Lu, L. Xia, K. Lin, D. Zou, Dose-dependent effects of strontium ranelate on ovariectomy rat bone marrow mesenchymal stem cells and human umbilical vein endothelial cells, *Int. J. Biol. Sci.* 12 (2016) 1511–1522, <https://doi.org/10.7150/ijbs.16499>.
- [37] A.L. Yerokhin, X. Nie, A. Leyland, A. Matthews, S.J. Dowe, Plasma electrolysis for surface engineering, *Surf. Coating. Technol.* 122 (1999) 73–93, [https://doi.org/10.1016/S0257-8972\(99\)00441-7](https://doi.org/10.1016/S0257-8972(99)00441-7).
- [38] Y.C. Fredholm, N. Karpukhina, D.S. Brauer, J.R. Jones, R.V. Law, R.G. Hill, Influence of strontium for calcium substitution in bioactive glasses on degradation, ion release and apatite formation, *J. R. Soc. Interface* 9 (2012) 880–889, <https://doi.org/10.1098/rsif.2011.0387>.
- [39] A. Karatrantos, R.J. Compsto, K.I. Winey, N. Clarke, Polymer and spherical nanoparticle diffusion in nanocomposites, *J. Chem. Phys.* 146 (2017) 203331, <https://doi.org/10.1063/1.4981258>.
- [40] D. Wang, J. Ye, T. Kako, T. Kimura, Photophysical and photocatalytic properties of SrTiO₃ doped with Cr cations on different sites, *J. Phys. Chem. B* 110 (2006) 15824–15830, <https://doi.org/10.1021/jp062487p>.
- [41] Y. Han, D.H. Chen, L. Zhang, Nanocrystallized SrHA/SrHA-SrTiO₃/SrTiO₃-TiO₂ multilayer coatings formed by micro-arc oxidation for photocatalytic application, *Nanotechnology* 19 (2008) 335705, <https://doi.org/10.1088/0957-4484/19/33/335705>.
- [42] H. Arcis, G.H. Zimmerman, P.R. Tremaine, Ion-pair formation in aqueous strontium chloride and strontium hydroxide solutions under hydrothermal conditions by AC conductivity measurements, *Phys. Chem. Chem. Phys.* 16 (2014) 17688–17704, <https://doi.org/10.1039/c4cp01703j>.
- [43] M. Sato, P. Chen, Y. Tsutsumi, M. Shioita, T. Hanawa, S. Kasugai, Effect of strontium ions on calcification of preosteoblasts cultured on porous calcium- and phosphate-containing titanium oxide layers formed by micro-arc oxidation, *Dent. Mater.* 32 (2016) 627–634, <https://doi.org/10.4012/dmj.2016-032>.
- [44] B. Wang, H. Guo, T. Geng, K. Sun, L. Zhang, Z. Lu, Q. Jin, The effect of strontium ranelate on titanium particle-induced preprothrotic osteolysis regulated by Wnt/ β -catenin signaling *in vivo* and *in vitro*, *Biosci. Rep.* 41 (2021), <https://doi.org/10.1042/BSR20203003>. BSR20203003.
- [45] S. Ali Akbari Ghavami, B.N. Allen, J.L. Stromsdorfer, J.S. Kramer, X. Li, B.D. Ulerly, Calcium and phosphate ions as simple signaling molecules with versatile osteoinductivity, *Biomed. Mater.* 13 (2018), 055005, <https://doi.org/10.1088/1748-605X/aac7a5>.
- [46] M.A. Riquelme, J.X. Jiang, Elevated intracellular Ca²⁺ signals by oxidative stress activate connexin 43 hemichannels in osteocytes, *Bone Res.* 1 (2013) 355–361, <https://doi.org/10.4248/BR201304006>.
- [47] K. Neha, M.R. Haider, A. Pathak, M.S. Yar, Medicinal prospects of antioxidants: a review, *Eur. J. Med. Chem.* 178 (2019) 687–704, <https://doi.org/10.1016/j.ejmech.2019.06.010>.
- [48] H.H. Qi, J. Bao, Q. Zhang, B. Ma, G.Y. Gu, P.L. Zhang, G. Ou-Yang, Z.M. Wu, H. J. Ying, P.K. Ou-Yang, Wnt/ β -catenin signaling plays an important role in the protective effects of FDP-Sr against oxidative stress induced apoptosis in MC3T3-E1 cell, *Bioorg. Med. Chem. Lett.* 26 (2016) 4720–4723, <https://doi.org/10.1016/j.bmcl.2016.08.043>.
- [49] M. Hayyan, M.A. Hashim, I.M. AlNashef, Superoxide ion: generation and chemical implications, *Chem. Rev.* 116 (2016) 3029–3085, <https://doi.org/10.1021/acs.chemrev.5b00407>.
- [50] S.Z.F. Phua, G. Yang, W.Q. Lim, A. Verma, H. Chen, T. Thanabal, Y. Zhao, Catalase-integrated hyaluronic acid as nanocarriers for enhanced photodynamic therapy in solid tumor, *ACS Nano* 13 (2019) 4742–4751, <https://doi.org/10.1021/acsnano.9b01087>.
- [51] Z.W. Zheng, Y.H. Chen, D.Y. Wu, J.B. Wang, M.M. Lv, X.S. Wang, J. Sun, Z. Y. Zhang, Development of an accurate and proactive immunomodulatory strategy to improve bone substitute material-mediated osteogenesis and angiogenesis, *Theranostics* 8 (2018) 5482–5500, <https://doi.org/10.7150/thno.28315>.
- [52] J. Bai, H. Wang, H. Chen, G. Ge, M. Wang, A. Gao, L. Tong, Y. Xu, H. Yang, G. Pan, P.K. Chu, D. Geng, Biomimetic osteogenic peptide with mussel adhesion and osteoimmunomodulatory functions to ameliorate interfacial osseointegration under chronic inflammation, *Biomaterials* 255 (2020) 120197, <https://doi.org/10.1016/j.biomaterials.2020.120197>.
- [53] X. Yin, C. Zhou, J. Li, R. Liu, B. Shi, Q. Yuan, S. Zou, Autophagy in bone homeostasis and the onset of osteoporosis, *Bone Res.* 7 (2019) 28, <https://doi.org/10.1038/s41413-019-0058-7>.
- [54] J. Tang, L. Chen, D. Yan, Z. Shen, B. Wang, S. Weng, Z. Wu, Z. Xie, J. Shao, L. Yang, L. Shen, Surface functionalization with proanthocyanidins provides an anti-oxidant defense mechanism that improves the long-term stability and osteogenesis of titanium implants, *Int. J. Nanomed.* 15 (2020) 1643–1659, <https://doi.org/10.2147/IJN.S231339>.
- [55] P.P. Souza, U.H. Lerner, The role of cytokines in inflammatory bone loss, *Immunol. Invest.* 42 (2013) 555–622, <https://doi.org/10.3109/08820139.2013.822766>.
- [56] C. Schlundt, T. El. Khassawna, A. Serra, A. Dienelt, S. Wendler, H. Schell, N. van Rooijen, A. Radbruch, R. Lucius, S. Hartmann, G.N. Duda, K. Schmidt-Bleek, Macrophages in bone fracture healing: their essential role in endochondral ossification, *Bone* 106 (2018) 78–89, <https://doi.org/10.1016/j.bone.2015.10.019>.
- [57] S.J. Zhao, F.Q. Kong, J. Jie, Q. Li, H. Liu, A.D. Xu, Y.Q. Yang, B. Jiang, D.D. Wang, Z.Q. Zhou, P.Y. Tang, J. Chen, Q. Wang, Z. Zhou, Q. Chen, G.Y. Yin, H.W. Zhang, J. Fan, Macrophage MSR1 promotes BMSC osteogenic differentiation and M2-like polarization by activating PI3K/AKT/GSK3 β / β -catenin pathway, *Theranostics* 10 (1) (2020) 17–35, <https://doi.org/10.7150/thno.36930>.
- [58] Q. Zhao, M. Shi, C. Yin, Z. Zhao, J. Zhang, J. Wang, K. Shen, L. Zhang, H. Tang, Y. Xiao, Y. Zhang, Dual-wavelength photosensitive nano-in-micro scaffold

- regulates innate and adaptive immune responses for osteogenesis, *Nano-Micro Lett.* 13 (1) (2020) 28, <https://doi.org/10.1007/s40820-020-00540-z>.
- [59] J. Zhang, H. Shi, N. Zhang, L. Hu, W. Jing, J. Pan, Interleukin-4-loaded hydrogel scaffold regulates macrophages polarization to promote bone mesenchymal stem cells osteogenic differentiation via TGF- β 1/Smad pathway for repair of bone defect, *Cell Prolif* 53 (2020), e12907, <https://doi.org/10.1111/cpr.12907>.
- [60] F. Zhao, B. Lei, X. Li, Y. Mo, R. Wang, D. Chen, X. Chen, Promoting *in vivo* early angiogenesis with sub-micrometer strontium-contained bioactive microspheres through modulating macrophage phenotypes, *Biomaterials* 178 (2018) 36–47, <https://doi.org/10.1016/j.biomaterials.2018.06.004>.
- [61] J. Muñoz, N.S. Akhavan, A.P. Mullins, B.H. Arjmandi, Macrophage polarization and osteoporosis: a review, *Nutrients Sep. 12* (2020) 2999, <https://doi.org/10.3390/nu12102999>.
- [62] P. Kazimierczak, M. Koziol, A. Przekora, The chitosan/agarose/NanoHA bone scaffold-induced M2 macrophage polarization and its effect on osteogenic differentiation *in vitro*, *Int. J. Mol. Sci.* 22 (2021) 1109, <https://doi.org/10.3390/ijms22031109>.
- [63] Y. Chen, M. Guan, R. Ren, C. Gao, H. Cheng, Y. Li, B. Gao, Y. Wei, J. Fu, J. Sun, W. Xiong, Improved immunoregulation of ultra-low-dose silver nanoparticle-loaded TiO₂ nanotubes via M2 macrophage polarization by regulating GLUT1 and autophagy, *Int. J. Nanomed.* 15 (2020) 2011–2026, <https://doi.org/10.2147/IJN.S242919>.